

AD-A235 324



2

PENNSTATE



Applied Research Laboratory

ACOUSTIC RADIATION FROM FLUID-LOADED, RIBBED CYLINDRICAL SHELLS EXCITED BY DIFFERENT TYPES OF CONCENTRATED MECHANICAL DRIVES

C. B. Burroughs and J. E. Hallander

Technical Memorandum
File No. 90-320
14 January 1991

Copy No. 3

DTIC
ELECTE
APR 30 1991
S C D

Approved for Public Release, Distribution Unlimited



Accession For	
DTIC GRAFI	<input checked="" type="checkbox"/>
DTIC TAB	<input type="checkbox"/>
Unannounced	<input type="checkbox"/>
Justification	
By _____	
Distribution/	
Availability Codes	
Dist	Avail and/or Special
A-1	

Applied Research Laboratory
P.O. Box 30
State College, PA 16804
(814) 865-3031

Contracted by the Department of the Navy
Space and Naval Warfare Systems Command
Contract No. N00039-88-C-0051

0 1 2 3 4 5 6 7 8 9

ACOUSTIC RADIATION FROM FLUID-LOADED, RIBBED CYLINDRICAL SHELLS EXCITED BY DIFFERENT TYPES OF CONCENTRATED MECHANICAL DRIVES

C. B. Burroughs and J. E. Hallander

Technical Memorandum
File No. 90-320
14 January 1991

Abstract: Analytic expressions are derived for the far field acoustic radiation from a fluid-loaded circular cylindrical shell reinforced with two sets of parallel periodic ribs and excited by seven types of mechanical point drives: single radial, in- and out-of-phase double radial, axial moment, circumferential moment, and in- and out-of-phase in-plane double circumferential. The ribs interact with the cylindrical shell only through normal forces. The model includes the effects of fluid loading, internal damping and interactions between ribs. Comparisons of predictions for the shell with a large radius are made to published results for unsupported and line-supported flat plates. Measurements of the acoustic radiation from a ribbed cylindrical shell excited by different types of drives are presented. Comparisons between measured and predicted results are made. Predictions of the acoustic radiation from the unsupported and supported shell with different types of drives are compared. The effects of properties of the shell and types of drives on the acoustic radiation are examined by example and some physical interpretation of significant features are offered.

Acknowledgements: The measurements were supported by the Office of Naval Research and the analytic model developed with support by Penn State Applied Research Laboratory E/F funding. The authors are grateful for this support and the computer programming assistance in processing the measured data provided by Marsha Mitchel, Mike Kronenwelter and Julie Laughton. The modeling was developed by J. E. Hallander in his thesis, submitted in partial fulfillment for his Masters Degree in Engineering Science at The Pennsylvania State University.

ORIGINALLY ISSUED AS AN IM 14 NOVEMBER 1990

The contractor, The Pennsylvania State University, hereby certifies that, to the best of its knowledge and belief, the technical data delivered herewith under Contract No. N00039-88-C-0051 is complete, accurate, and complies with all requirements of the contract.

Date: 14 January 1991

Name and Title of Certifying Official: _____


Dr. L. R. Hettche, Project Director

TABLE OF CONTENTS

	<u>Page Number</u>
ABSTRACT	1
LIST OF TABLES	4
LIST OF FIGURES	4
1.0 INTRODUCTION	8
2.0 DESCRIPTION OF ANALYTIC MODEL	14
2.1 Shell Equations	16
2.2 Fluid Loading	18
2.3 The Rings	19
2.4 Solution for Transverse Drives	21
2.5 Solution for Circumferential In-Plane Drives	22
2.6 The Driving Force	22
2.6.1 Single Radial Drive	23
2.6.2 The Double Radial Drive	24
2.6.3 The Circumferential Moment Drive	24
2.6.4 The Axial Moment Drive	25
2.6.5 The Circumferential In-Plane Drives	26
2.7 Acoustic Radiation	26
3.0 DESCRIPTION OF MEASUREMENTS	27
3.1 The Shell	28
3.2 Shaker Configurations	28
3.3 Measurement Configuration and Instrumentation	29
3.4 Data Reduction	30

TABLE OF CONTENTS (CONTINUED)

	<u>Page Number</u>
4.0 VALIDATION OF ANALYTIC MODEL	32
4.1 Comparison to Published Results	33
4.2 Predictions versus Measurements	33
5.0 NUMERICAL RESULTS	39
6.0 CONCLUSIONS	49
REFERENCES	51
TABLE	54
FIGURES	55

LIST OF TABLES

<u>Table Number</u>	<u>Title</u>	<u>Page Number</u>
1	Parameters Used in Shell Model	54

LIST OF FIGURES

<u>Figure Number</u>	<u>Title</u>	<u>Page Number</u>
1	Geometry and Coordinate System for Doubly Periodic Ribbed Circular Cylindrical Shell	55
2	Radial and Moment Drives	56
3	In-Plane Circumferential Drives	57
4	Section of Shell Used in Measurements	58
5	Shaker Mounting Arrangement for Circumferential Moment Drive	59
6	Shaker Mounting Arrangement for Longitudinal In-Plane Drives	60
7	Comparisons of Predictions of Acoustic Radiation from an Unsupported Cylindrical Shell with a Large Radius to Published Predictions for an Unsupported Flat Plate	61
8	Comparison of Predictions of Acoustic Radiation from a Cylindrical Shell with Single Periodic Ribs and Large Radius to Published Predictions for Flat Plate with Single Periodic Line Supports	62
9	Comparison of Predictions of Acoustic Radiation from a Cylindrical Shell with Doubly Periodic Ribs and Large Radius to Published Predictions for Flat Plate with Doubly Periodic Line Supports	63
10	Comparison of Predicted and Measured Acoustic Radiation from Ribbed Cylindrical Shell Excited by Single Radial Drive	64
11	Comparison of Predicted and Measured Acoustic Radiation from Ribbed Cylindrical Shell Excited by Out-of-Phase Double Radial Drive	65

LIST OF FIGURES (CONTINUED)

<u>Figure Number</u>	<u>Title</u>	<u>Page Number</u>
12	Comparison of Predicted and Measured Acoustic Radiation from Ribbed Cylindrical Shell Excited by In-Phase Double Radial Drive	66
13	Comparison of Predicted and Measured Acoustic Radiation from Ribbed Cylindrical Shell Excited by Axial Moment Drive	67
14	Comparison of Predicted and Measured Acoustic Radiation from Ribbed Cylindrical Shell Excited by Circumferential Moment Drive	68
15	Comparison of Predicted and Measured Acoustic Radiation from Ribbed Cylindrical Shell Excited by Out-of-Phase In-Plane Circumferential Drive	69
16	Comparison of Predicted and Measured Acoustic Radiation from Ribbed Cylindrical Shell Excited by In-Phase In-Plane Circumferential Drive	70
17	Acoustic Radiation from Doubly-Periodic Ribbed Shell with and without Damping for a Single Radial Drive	71
18	Acoustic Radiation from Doubly-Periodic Ribbed Shell with and without Damping for an Out-of-Phase Double Radial Drive . .	72
19	Acoustic Radiation from Doubly-Periodic Ribbed Shell with and without Damping for a Circumferential Moment Drive	73
20	Acoustic Radiation from Doubly-Periodic Ribbed Shell with and without Damping for an Out-of-Phase In-Plane Circumferential Drive	74
21	Acoustic Radiation from Shell with No Ribs, Singly-Periodic Ribs and Doubly-Periodic Ribs for Single Radial Drive	75

LIST OF FIGURES (CONTINUED)

<u>Figure Number</u>	<u>Title</u>	<u>Page Number</u>
22	Acoustic Radiation from Shell with No Ribs, Singly-Periodic Ribs and Doubly-Periodic Ribs for Out-of-Phase Double Radial Drive	76
23	Acoustic Radiation from Shell with No Ribs, Singly-Periodic Ribs and Doubly-Periodic Ribs for Circumferential Moment Drive	77
24	Acoustic Radiation Directivity for Shell with No Ribs, Singly-Periodic Ribs and Doubly-Periodic Ribs for Axial Moment Drive	78
25	Acoustic Radiation Directivity for Doubly-Periodic Ribbed Shell for Axial Moment Drive at Different Locations	79
26	Acoustic Radiation from Shell with No Ribs, Singly-Periodic Ribs and Doubly-Periodic Ribs for In-Phase, In-Plane Circumferential Drive	80
27	Acoustic Radiation from Shell with No Ribs, Singly-Periodic Ribs and Doubly-Periodic Ribs for Out-of-Phase, In-Plane Circumferential Drive	81
28	Acoustic Radiation Directivity for Shell with Singly- and Doubly-Periodic Ribs for Single Radial Drive	82
29	Acoustic Radiation Directivity for Doubly-Periodic Ribbed Shell for Single Radial and Axial Moment Drives	83
30	Acoustic Radiation Directivity for Shell with Singly- and Doubly-Periodic Ribs for In-Phase, In-Plane Circumferential Drive .	84
31	Acoustic Radiation from Doubly-Periodic Shell with Different Radii for Circumferential Moment Drive	85
32	Acoustic Radiation from Singly-Periodic Ribbed Shell for Single Radial, Double In-Plane and Out-of-Phase Radial, and Circumferential Moment Drives	86

LIST OF FIGURES (CONTINUED)

<u>Figure Number</u>	<u>Title</u>	<u>Page Number</u>
33	Acoustic Radiation from Doubly-Periodic Ribbed Shell for Single Radial and Double In-Phase and Out-of-Phase Radial Drives . .	87
34	Acoustic Radiation from Doubly-Periodic Ribbed Shell for Single Radial, and Axial and Circumferential Moment Drives	88
35	Acoustic Radiation from Doubly-Periodic Ribbed Shell for Single Radial, and Circumferential In- and Out-of-Phase, In-Plane Drives	89

1.0 INTRODUCTION

Structures reinforced by ribs are often mechanically excited and are thereby sources of acoustic radiation. The amount of acoustic radiation is affected by the response of the structure to mechanical excitation and the radiation efficiency of the structure. At lower frequencies and/or for lightly damped structures, where the modal overlap is small in finite structures, the vibration response and consequently the acoustic radiation is strongly influenced by resonances in the structure. At higher frequencies and/or for heavily damped structures, where modal overlap is large, the response of finite structures approximates the response of infinite structures of the same configuration. In this case, the peaks in the acoustic radiation are generated by rib supports which alter the response of the structure to increase the acoustic coupling of the structural response to the acoustic radiation. In addition to resonant responses and rib-structure interaction, the acoustic radiation at all frequencies is influenced by the type of mechanical excitation.

In this paper, an analytic model is developed and exercised for the acoustic radiation from fluid-loaded, infinite ribbed circular cylindrical shells excited by different types of concentrated mechanical drives to address the influence that ribs and the type of mechanical drive have on acoustic radiation. To validate the model, predicted levels of the far field acoustic radiation are compared to levels measured on a finite ribbed shell excited mechanically with different types of drives. Because the shell used in the measurements had a finite length, resonances in the vibration response are present which produced peaks in the acoustic radiation levels not seen in the

predicted levels for an infinite shell. However, radiation from the structural near field of the localized drives and scattering of waves in the shell by ribs will be present in both the measured and predicted radiated noise levels. Therefore, when the resonance effects are identified in the measurements, verification of the analytic model with measurements can be performed. Once validated with measurements, the analytic model is exercised to explore the influence that ribs and different types of mechanical drives have on the acoustic radiation from fluid-loaded, ribbed cylindrical shells.

Most of the published studies on the acoustic radiation from ribbed structures have concentrated on point-driven flat infinite plates. Maidanik [1] was one of the first to investigate the effects of stiffeners on the acoustic radiation from plates. His results showed that the addition of periodic rigid rib stiffeners to flat plates increased the radiation efficiency at frequencies below the critical frequency of the plate. Lyon [2] and Nayak [3] studied the radiation efficiency of a flat infinite plate reinforced by a single elastic beam at frequencies below the critical frequency. Lyon showed that the acoustic radiation decreased as the transverse motion of the beam increased, i.e. as the beam impedance decreased. Nayak added fluid-loading to Lyon's model and found that the radiation efficiency decreased as the fluid-loading increased. Maidanik [4] considered the influence of plate rib reinforcements on acoustic radiation in terms of the conversion of wavenumber spectra in the plate by the ribs where he showed that the ribs converted vibration responses at high wavenumbers into responses at low wavenumbers which couple better to acoustic radiation. Directivity patterns associated with radiation produced by a

rigid beam attached to a plate are presented by Belinskii [5]. Simple expressions for the radiation from a beam reinforced infinite plate modeled by a membrane with frequency dependent tension are derived by Crighton and Maidanik [6]. The influence of longitudinal and flexural vibration of a reinforcing beam on radiation from an infinite plate are considered by Evseev and Kirpichnikov [7]. Below the critical frequency of the plate, the radiation associated with the longitudinal vibrations of the beam have more influence on acoustic radiation than the flexural vibration of the beam, according to Evseen and Kirpichnikov. Lin and Hayek [8] showed that the radiation decreased with increases in the size of the beam at frequencies below the critical frequency of the plate.

Using energy methods, radiation from an infinite plate supported by two beams was considered by Romanov [9]. Reflections from the beams and force and moment rib impedances were included in Romanov's analysis. The acoustic radiation from an infinite plate supported by two beams with randomly distributed forces applied to the plate between the beams was considered by Svyatenko [10]. Garrellick and Lin [11] presented results on the influence of the number of ribs on radiation from a plate driven by a point source. The plate radiation was affected more by the number of ribs at low frequencies. At higher frequencies, the effect of the number of ribs decreased. An infinite plate reinforced by a finite set of beams was considered by Romanov [12]. Moment and force impedances of the beams were included in Romanov's analysis. The beams closest to the point drive were shown to have the greatest effect on the radiation from the plate. The reactive moments of the beam to plate displacements were also shown to have a significant effect on acoustic radiation.

Romanov [13] and Evseev [14] added an infinite set of periodically-spaced elastic line supports to a point-driven flat infinite plate. They concluded that peaks in the acoustic radiation were caused by resonances in the plate sections between the supports. Mace [15] investigated a point-driven flat infinite plate stiffened by two parallel sets of periodic elastic line supports. According to Mace, the peaks in the acoustic radiation at frequencies below the critical frequency were due to the coherent addition of radiation at the locations of the line supports where the line supports produce local radiation. The acoustic radiation from a plate reinforced by two sets of periodically-spaced orthogonal ribs was considered by Mace [16]. Using an energy approach, Mead and Mallik [17] developed a model for the acoustic radiation from an infinite plate reinforced by periodic rib supports. Plakhov [18] applied reciprocity and eigenfunction expansions for the plates between rigid supports to investigate the acoustic radiation from rib reinforced plates. At resonances, the radiation was higher for the supported plate than for the unsupported plate. At the anti-resonances of the plates between the supports, the radiation was lower for the supported plate than for the unsupported plate. Vyalyshv and Tantakovskii [19] investigated the reduction of the acoustic radiation from a ribbed infinite plate by the addition of a second line source to the plate.

In flat plates, the transverse vibrations can be treated separately from the in-plane vibrations. Adding curvature couples the in-plane and transverse vibrations which has a significant effect on the wavenumber spectra of the vibration response and consequently the radiation of the structure. Curvature with a constant radius in one direction is added

when circular cylindrical shells are considered. To include the effects of curvature and increase the applicability of analytic models to realistic structures, there have been a number of investigations that have tackled the increased complexity introduced by structural curvature to explore the acoustic radiation from ribbed cylindrical shells.

Bernblit examined the acoustic radiation from a point-driven infinite circular cylinders stiffened by two [20] and five [21] equally-spaced ring supports. Bernblit approximated the ring impedance by a pure mass reactance. Numerical results presented for the unsupported cylinder and the cylinder supported by two rings showed peaks at the resonance frequencies associated with the shell segments between the ring supports. Bernblit included damping in his model and showed a decrease in the peak acoustic radiation as damping increased. Ribbed cylindrical shells with small curvature were considered by Ivanov and Romanov [22] at frequencies above the shell ring frequency and below the critical frequency of the shell. An energy approach was employed where average transmission losses were applied to each of the identical, finite number of ribs. A finite number of ribs was also considered by Lawrie [23], who modeled the ribs as rigid supports for axisymmetric excitation on the shell. Ribbed shells were divided by El-Raheb and Wagner [24] into segments between the reinforcing ribs. The segments were coupled by means of impedance matrices for the ribs. The in-plane and out-of-plane motions of the ribs were assumed by El-Raheb and Wagner to decouple. The radiation from a ribbed cylindrical shell excited by an internal monopole acoustic source was considered by Fuller [25]. Fuller uncovered nonradiating energy that propagated along the surface of the shell. A three layer shell model was employed by Reddy and

Mallik [26] to model a ribbed cylindrical shell with constrained layer damping added to the shell surface. Numerical results with three rigid supports were presented for shell excitation by an internal acoustic source. The acoustic radiation from point-driven fluid-loaded cylindrical shells supported by doubly-periodic ring supports was studied by Burroughs [27]. Two mechanisms of radiation at frequencies below the critical frequency were identified: (a) radiation from the structural near field of the point drive and (b) scattering of vibrational energy in the shell by the rings. Burroughs also showed that structural damping reduced peaks in the acoustic radiation.

In all of the above referenced publications, the plate or shell was excited by radial forces. The acoustic radiation from moment-driven structures has not received as much attention in published studies as structures excited by radial point forces. Thompson and Rattayya [28] investigated the acoustic radiation from a moment-drive flat unsupported infinite plate with and without fluid loading. For light fluid loading, the acoustic radiation efficiency of moment-driven plates is less than for point-driven plates, and unlike point-driven plates, is frequency dependent below the critical frequency. Their results showed that, for frequencies below the critical frequency, increasing the fluid loading reduced the acoustic radiation efficiency of moment-driven plates. Feit [29] investigated the far field acoustic radiation from a moment-driven unsupported flat infinite plate above and below the critical frequency. He found the radiation pattern to be nondirectional and insensitive to structural damping at frequencies below the critical frequency. Above the critical frequency, Feit reported the radiation pattern to be directive and that peaks in the radiating patterns can be reduced by

increased damping. The authors of this paper are not aware of any publications on the acoustic radiation from ribbed structures excited by other than radial point or distributed drives.

The derivation of the mathematical equations and their solutions for the far field acoustic radiation from infinite fluid-loaded cylindrical shells supported by two sets of parallel periodic ring supports excited by radial, moment and in-plane drives are presented in Section 2.0. Measurements conducted on a ribbed cylindrical shell in water driven by mechanical shakers, configured to generate concentrated radial, in-plane and moment drives, are described in Section 3.0. To validate the analytic model, numerical results for the far field acoustic radiation from the cylinder with a large radius are compared in Section 4.0 to published results for flat infinite plates. Also, in Section 4.0, numerical results from the analytic model are compared to measured data taken on the ribbed cylindrical shell described in Section 3.0. Once validated with published and measured data under common conditions, the analytic model is exercised in Section 5.0 for different shell properties and types of mechanical concentrated localized drives. Conclusions and a summary are given in Section 6.0.

2.0 DESCRIPTION OF ANALYTIC MODEL

An infinite, thin, circular, cylindrical shell of thickness h and radius a is centered on the x -axis as shown in Figure 1. The shell is stiffened with two sets of periodically spaced rings attached to the inside surface of the shell. The first set of rings (smaller rings) have a periodic spacing of d . The second set of rings (larger rings) are separated by $N-1$ smaller rings so that the periodic spacing of the

second set is Nd. The interior of the shell is in a vacuum. The shell is surrounded by a fluid of density ρ_0 , and acoustic phase velocity c_0 . As shown in Figure 1, the observation point is located at a distance R, a polar angle θ from the centerline of the shell (x-axis), and an azimuthal angle ϕ .

The derivation of the shell vibration and acoustic radiation equations, given below, follows that given by Burroughs [27]. In this derivation, the following assumptions are made:

- (1) All the derivations have implicit $e^{-i\omega t}$ harmonic time dependence, where ω is the radian frequency.
- (2) The pressure on the shell, and the radial displacements are positive when directed outward from the center of the shell.
- (3) Thin bending cylindrical shell theory, which is a refinement of Timoshenko's theory by Kennard [30], is used to describe the motion of the shell.
- (4) The external driving forces are applied at points on the middle surface of the shell.
- (5) Shear and bending interactions between the ring supports and the shell are ignored so the rings apply only normal reactive forces to the middle surface of the shell along the circular line of intersection of the shell and ring.
- (6) The observation point for the acoustic radiation is located in the far field, such that $k_0 R \gg 1$, where k_0 is the acoustic wavenumber and R is the radial distance from the center of the shell.

2.1 Shell Equations

With the above assumptions, the equations of motion for an infinite circular cylindrical shell reinforced by doubly-periodic circular rings are

$$\begin{aligned}
 & \frac{\partial^2 \dot{u}}{\partial x^2} + \frac{1-\nu}{2a^2} \frac{\partial^2 \dot{u}}{\partial \phi^2} + \frac{1+\nu}{2a} \frac{\partial^2 \dot{v}}{\partial x \partial \phi} + \frac{\nu}{a} \frac{\partial \dot{w}}{\partial x} + k_t^2 \dot{u} = CF_1 \\
 & \frac{1+\nu}{2a} \frac{\partial^2 \dot{u}}{\partial x \partial \phi} + \frac{1}{a^2} \frac{\partial^2 \dot{v}}{\partial \phi^2} + \frac{1-\nu}{2} \frac{\partial^2 \dot{v}}{\partial x^2} + \frac{1}{a^2} \frac{\partial \dot{w}}{\partial \phi} \\
 & + \frac{h^2 \nu}{8(1-\nu)a^4} \left(\frac{\partial \dot{w}}{\partial \phi} + \frac{\partial^3 \dot{w}}{\partial \phi^3} \right) + k_t^2 \dot{v} = CF_2 \\
 & \frac{\nu}{a} \frac{\partial \dot{u}}{\partial x} + \frac{1}{a^2} \frac{\partial \dot{v}}{\partial \phi} + \frac{\dot{w}}{a^2} \\
 & + \frac{h^2}{24(1-\nu)} \left[2(1-\nu) \left(\frac{\partial^2}{\partial x^2} + \frac{1}{a^2} \frac{\partial^2}{\partial \phi^2} \right)^2 \dot{w} + \frac{4-\nu}{a^4} \frac{\partial^2 \dot{w}}{\partial \phi^2} + \frac{2+\nu}{a^4} \dot{w} \right] - k_t^2 \dot{w} \\
 & = CF_3
 \end{aligned} \tag{1}$$

where a is the shell radius, h is the shell thickness, ν is Poisson's ratio, $k_t = \omega/c_t$, $c_t = [E/\rho(1-\nu^2)]^{1/2}$ is the longitudinal wavespeed, ρ is the volume density of the shell material and E is Young's modulus. The constant, C , is

$$C = \frac{-i\omega}{\rho c_t^2} \left[\frac{1}{h} + \frac{1-2\nu}{2a(1-\nu)} \right] \tag{2}$$

where $i = \sqrt{-1}$

The symbols \dot{u} , \dot{v} , and \dot{w} are the time derivatives of the axial in-plane, circumferential in-plane and the radial shell displacements respectively. The pressure terms F_i are

$$\begin{aligned}
 F_1 &= f_1(x, \phi) \\
 F_2 &= f_2(x, \phi) \\
 F_3 &= f_3(x, \phi) - p^f(x, \phi) - p^r(x, \phi) - p^b(x, \phi)
 \end{aligned} \tag{3}$$

where f_1 , f_2 and f_3 are the pressures applied to the shell by an axial in-plane drive, a circumferential in-plane drive, and a transverse drive, respectively. The pressure due to the fluid loading is p^f and the pressures exerted by the first and second set of rings are p^r and p^b respectively. Taking the Fourier transform of Equations (1), where the transform is defined as

$$\tilde{f}(k, \phi) = \frac{1}{2\pi} \int_{-\infty}^{\infty} f(x, \phi) e^{-ikx} dx, \quad (4)$$

with the corresponding inverse

$$f(x, \phi) = \int_{-\infty}^{\infty} \tilde{f}(k, \phi) e^{ikx} dk, \quad (5)$$

and substituting solutions of the form:

$$\begin{aligned} \tilde{u}(k, \phi) &= \sum_{n=-\infty}^{\infty} \tilde{u}_n(k) e^{in\phi}, \quad \tilde{v}(k, \phi) = \sum_{n=-\infty}^{\infty} \tilde{v}_n(k) e^{in\phi}, \\ \tilde{w}(k, \phi) &= \sum_{n=-\infty}^{\infty} \tilde{w}_n(k) e^{in\phi}, \quad \tilde{f}_1(k, \phi) = \sum_{n=-\infty}^{\infty} \tilde{f}_n(k) e^{in\phi}, \\ \tilde{f}_2(k, \phi) &= \sum_{n=-\infty}^{\infty} \tilde{f}_n(k) e^{in\phi}, \quad \tilde{f}_3(k, \phi) = \sum_{n=-\infty}^{\infty} \tilde{f}_n(k) e^{in\phi}, \\ \tilde{p}^f(k, \phi) &= \sum_{n=-\infty}^{\infty} \tilde{p}_n^f(k) e^{in\phi}, \quad \tilde{p}^r(k, \phi) = \sum_{n=-\infty}^{\infty} \tilde{p}_n^r(k) e^{in\phi}, \\ \tilde{p}^b(k, \phi) &= \sum_{n=-\infty}^{\infty} \tilde{p}_n^b(k) e^{in\phi}, \end{aligned} \quad (6)$$

yields

$$\tilde{Z}_n^s(k) \tilde{w}_n(k) = -\tilde{D}_n(k) \tilde{f}_{2n} + \tilde{f}_{3n} - \tilde{p}_n^f - \tilde{p}_n^r - \tilde{p}_n^b \quad (7)$$

where $\tilde{D}_n(k)$ is

$$\tilde{D}_n(k) = \frac{in \left[\Omega^2 - \alpha^2 \left(\frac{1-v^2}{2} \right) - n^2 \left(\frac{1-v}{2} \right) \right]}{[-\Omega^2 + \alpha^2 + n^2] \left[-\Omega^2 + \left(\frac{1-v}{2} \right) (\alpha^2 + n^2) \right]} \quad (8)$$

and the shell impedance for the n^{th} circumferential mode is

$$\begin{aligned}
\tilde{Z}_n^s(k) = & \frac{i\rho C_1^2}{\omega a^2 \left\{ \frac{1}{h} + (1-2\nu)/[2a(1-\nu)] \right\}} \left[-\Omega^2 + \frac{h^2}{24a^2(1-\nu)} \right. \\
& [2(1-\nu)(n^2 + \alpha^2)^2 - n^2(4-\nu) + 2 + \nu] + \\
& \frac{\alpha^2(1-\nu^2) \left[\frac{1}{2}(1-\nu)\alpha^2 - \Omega^2 \right] - \Omega^2 \left[\frac{1}{2}(1-\nu)(\alpha^2 + n^2) - \Omega^2 \right]}{\left[\frac{1}{2}(1-\nu)(\alpha^2 + n^2) - \Omega^2 \right] [\alpha^2 + n^2 - \Omega^2]} + \quad (9) \\
& \left. \frac{\frac{h^2}{8a^2(1-\nu)} n^2(1-n^2) \left(a^2\nu \frac{1+\nu}{2} + \Omega^2 - \alpha^2 - \frac{1-\nu}{2} n^2 \right)}{\left[\frac{1}{2}(1-\nu)(\alpha^2 + n^2) - \Omega^2 \right] [\alpha^2 + n^2 - \Omega^2]} \right].
\end{aligned}$$

where $\Omega = \omega a/c_t$ and $\alpha = ka$

In Equation (7), we have ignored the axial in-plane drives given by F_1 , since the axial in-plane motion couples poorly to the radial motion of the shell and consequently should produce little acoustic radiation.

2.2 Fluid Loading

The acoustic pressure in the fluid surrounding the shell satisfies the Helmholtz equation

$$\nabla^2 p^f + k_o^2 p^f = 0, \quad (10)$$

where k_o is the acoustic wavenumber and the ∇^2 operator is defined as

$$\nabla^2 = \frac{1}{r} \left(\frac{\partial}{\partial r} \frac{1}{r} \frac{\partial}{\partial r} \right) + \frac{1}{r^2} \frac{\partial^2}{\partial \phi^2} + \frac{\partial^2}{\partial x^2}. \quad (11)$$

Taking the Fourier transform on x in Equation (10) and solving the resulting equation yields

$$p^f(r, k, \phi) = \sum_{n=-\infty}^{\infty} A_n H_n^{(1)}[(k_o^2 - k^2)^{1/2} r] e^{in\phi}, \quad (12)$$

where $H_n^{(1)}$ is the Hankel function of the first kind and order n . To find the constants A_n , the continuity of the radial displacement at the shell/fluid boundary is used, i.e.,

$$\frac{\partial p^f}{\partial r} \Big|_{r=a} = i\rho\omega\dot{w} . \quad (13)$$

Applying the Fourier transform and using Equation (6), the pressure at the shell surface becomes

$$\tilde{p}^f(a, k, \phi) = \sum_{n=-\infty}^{\infty} \tilde{Z}_n^f(k) \tilde{w}_n(k) e^{in\phi} , \quad (14)$$

where \tilde{Z}_n^f is the acoustic impedance for the n^{th} circumferential mode given by

$$\tilde{Z}_n^f = \frac{i\rho\omega H_n^{(1)}[(k_o^2 - k^2)^{1/2}a]}{(k_o^2 - k^2)^{1/2} H_n^{(1)'}[(k_o^2 - k^2)^{1/2}a]} . \quad (15)$$

In Equation (15), $H_n^{(1)'}$ is the derivative of the Hankel function with respect to the argument. Comparing Equation (14) with Equation (6) yields

$$\tilde{p}_n^f(k) = \tilde{Z}_n^f(k) \tilde{w}_n(k) . \quad (16)$$

2.3 The Rings

The pressure applied to the shell by the first set of rings can be modeled by

$$p^r(a, \phi) = \bar{p}^r(\phi) \sum_{m=-\infty}^{\infty} \delta(x - md) , \quad (17)$$

where d is the periodic spacing of the rings, and $p^r(a, \phi)$ is the pressure per unit length applied by a ring to the shell in a direction normal to the shell surface. The equations of motion that describe the dynamics of the rings are derived from Equations (1) by letting $\dot{u}(x, \phi) = 0$, $\dot{v}(x, \phi) = \dot{v}(\phi)$, $\dot{w}(x, \phi) = \dot{w}(\phi)$, and Poisson's ratio = 0.

By assuming solutions of the form

$$\dot{v}' = \sum_{n=-\infty}^{\infty} \dot{v}'_n e^{in\theta}, \quad \dot{w}' = \sum_{n=-\infty}^{\infty} \dot{w}'_n e^{in\theta}, \quad \dot{p}' = \sum_{n=-\infty}^{\infty} \dot{p}'_n e^{in\theta}, \quad (18)$$

the pressure applied by the first set of rings for the n^{th} circumferential mode is given by [28]

$$\dot{p}'_n(k) = \frac{k_d}{2\pi} Z_n^r \sum_{m=-\infty}^{\infty} \tilde{w}'_m(k - mk_d) \quad (19)$$

where

$$Z_n^r = \frac{i}{\omega a} \left(\frac{2\rho_r A_r c_l'^2}{2a + h_r} \right) \cdot \left[1 + \frac{h_r^2}{12a^2} (n^2 - 1)^2 - \Omega^2 + \frac{n^2}{\Omega^2 - n^2} \right] \quad (20)$$

and

$$k_d = 2\pi/d \quad (21)$$

In Equation (20), ρ_r is the volume density of the ring material, h_r is the thickness of the ring, c_l' is the longitudinal wavespeed in the ring, and A_r is the cross-sectional area of the ring.

For the second set of rings, the pressure is given by

$$\dot{p}_n^b(k) = \frac{k_D}{2\pi} (Z_n^b - Z_n^r) \sum_{m=-\infty}^{\infty} \tilde{w}'_m(k - mk_D) \quad (22)$$

where $k_D = 2\pi/D$. $D = Nd$ is the spacing of the second set of rings and Z_n^b is the impedance for a ring in the second set of rings and is given by Equation (20). The rings of the second set of rings are located at every N^{th} ring in the first set so that, as shown in Equation (22), it is necessary at these locations to subtract the impedance of the ring in the first set from the impedance of the ring in the second set.

2.4 Solution for Transverse Drives

For the four transverse driving forces shown in Figure 2, $\tilde{f}_{2n} = 0$ in Equation (7). Using this along with Equations (16), (19) and (22) in Equation (7) yields

$$\tilde{z}_n^s(k) \tilde{w}_n(k) = \tilde{f}_{3n} - Z_n^r \tilde{w}_n - Z_n^r S_d \{ \tilde{w}_n \} - (Z_n^b - Z_n^r) S_D \{ \tilde{w}_n \} , \quad (23)$$

where the operators $S_d ()$ and $S_D ()$ are as follows

$$S_d \{ A(k) \} = \frac{k_d}{2\pi} \sum_{m=-\infty}^{\infty} A(k - mk_d) , \quad (24)$$

$$S_D \{ A(k) \} = \frac{k_D}{2\pi} \sum_{m=-\infty}^{\infty} A(k - mk_D) . \quad (25)$$

Equation (23) can be rewritten as

$$\tilde{w}_n(k) = \tilde{Y}_n \tilde{f}_{3n} - \tilde{Y}_n Z_n^r S_d \{ \tilde{w}_n \} - \tilde{Y}_n (Z_n^b - Z_n^r) S_D \{ \tilde{w}_n \} \quad (26)$$

where the fluid-loaded shell admittance is,

$$\tilde{Y}_n = (\tilde{Z}_n^s + \tilde{Z}_n^f)^{-1} \quad (27)$$

Solving Equation (26) for \tilde{w}_n yields [9]

$$\tilde{w}_n = \tilde{Y}_n \left[\tilde{f}_{3n} - Z_n^r \frac{S_d \{ \tilde{Y}_n \tilde{f}_{3n} \}}{1 + Z_n^r S_d \{ \tilde{Y}_n \}} - \frac{Z_n^b - Z_n^r}{1 + Z_n^r S_d \{ \tilde{Y}_n \}} \right. \\ \left. \frac{1}{2N-1} \sum_{p=N+1}^{N-1} \left[\frac{S_d \{ \tilde{f}_{3n}(k - pk_D) \} \tilde{Y}_n(k - pk_D)}{1 + Z_n^r S_d \{ \tilde{Y}_n(k - pk_D) \}} \right] \right] \\ \left. 1 + \frac{Z_n^b - Z_n^r}{2N-1} \sum_{p=N-1}^{N-1} \left[\frac{S_d \{ \tilde{Y}_n(k - pk_D) \}}{1 + Z_n^r S_d \{ \tilde{Y}_n(k - pk_D) \}} \right] \right] , \quad (28)$$

where $k_d = Nk_D$. There are three terms in Equation (28). The first term represents the solution for an unsupported shell. The second term represents the reactive forces due to the first set of rings and is periodic in k , with a period k_d . The third term represents the reactive forces due to the second set of rings and is periodic in k with period k_D .

2.5 Solution for Circumferential In-Plane Drives

For the circumferential in-plane drive considered here, as shown in Figure 3, $f_{3n} = 0$ in Equation (7) so that

$$\tilde{z}_n^s(k) \tilde{w}_n(k) = \tilde{D}_v \tilde{f}_{2n} - \tilde{p}_n^f - \tilde{p}_n^r - \tilde{p}_n^b. \quad (29)$$

Following the procedure used in Section 2.4 for the transverse drives yields the solution for the radial velocity distribution due to a circumferential in-plane drive:

$$\begin{aligned} \tilde{w}_n = - \tilde{Y}_n & \left[\tilde{D}_n \tilde{f}_{2n} - Z_n^r \frac{S_d\{\tilde{Y}_n \tilde{D}_v \tilde{f}_{2n}\}}{1 + Z_n^r S_d\{\tilde{Y}_n\}} - \frac{Z_n^b - Z_n^r}{1 + Z_n^r S_d\{\tilde{Y}_n\}} \right. \\ & \left. \frac{1}{2N-1} \sum_{p=-N+1}^{N-1} \frac{S_d\{\tilde{D}_v(k - pk_D) \tilde{f}_{2n}(k - pk_D) \tilde{Y}_n(k - pk_D)\}}{1 + Z_n^r S_d\{\tilde{Y}_n(k - pk_D)\}} \right. \\ & \left. \frac{1}{1 + \frac{Z_n^b - Z_n^r}{2N-1} \sum_{p=-N+1}^{N-1} \frac{S_d\{\tilde{Y}_n(k - pk_D)\}}{1 + Z_n^r S_d\{\tilde{Y}_n(k - pk_D)\}}} \right] \quad (30) \end{aligned}$$

2.6 The Driving Force

In addition to the single radial drive, for which results are given by Burroughs [28], expressions are derived in this section for four transverse drives and two circumferential in-plane drives. The transverse drives are in-phase and out-of-phase double radial drives, axial moment drive, and circumferential moment drive. The in-plane drives are in-phase and out-of-phase double circumferential drives. These drives are illustrated in Figures 2 and 3.

Since shear forces and moments applied by the support rings to the shell are ignored and there is no shell curvature in the axial direction, the mechanisms in the analytic model given here for the conversion of the shell response to the in-plane axial drive to the radial response necessary for acoustic radiation is weak. Therefore, axial in-plane drives are not treated in this paper.

2.6.1 Single Radial Drive

The pressure applied by a single radial drive at a point (x_0, ϕ_0) is given by

$$f_3(x, \phi) = F \delta(x - x_0) \sum_{m=-\infty}^{\infty} \delta[a\{\phi - (\phi_0 + 2\pi m)\}] , \quad (31)$$

where F is the magnitude of the driving force and δ is the zeroth order Dirac delta function. At $x_0 = 0$, the drive location is at one of the rings in the second set of rings. Note that the expression for the applied force has the required spatial periodicity in ϕ of 2π . Applying the Fourier transform on x gives

$$\tilde{f}_{3n}(k, \phi) = \frac{Fe^{-ikx_0}}{2\pi} \sum_{m=-\infty}^{\infty} \delta[a\{\phi - (\phi_0 + 2\pi m)\}] . \quad (32)$$

Applying Poisson's summation formula, Equation (32) reduces to

$$\tilde{f}_{3n}(k, \phi) = \frac{Fe^{-ikx_0}}{(2\pi)^2 a} \sum_{n=-\infty}^{\infty} e^{in(\phi - \phi_0)} . \quad (33)$$

Comparing this with Equation (6) gives

$$\tilde{f}_{3n}(k) = \frac{F}{(2\pi)^2 a} e^{-i(kx_0 + n\phi_0)} . \quad (34)$$

2.6.2 The Double Radial Drive

For the double radial point drive, one point drive is located at (x_0, ϕ_0) , with the second drive located at $(x_0, \phi_0 + \pi)$. The expression for the applied pressure from the double radial drive is

$$f_{3n}(x, \phi) = F \delta(x - x_0) \left[\sum_{n=-\infty}^{\infty} \delta(a[\phi - (\phi_0 + 2\pi n)]) \pm \sum_{n=-\infty}^{\infty} \delta(a[\phi - (\phi_0 + \pi + 2\pi n)]) \right] . \quad (35)$$

The positive sign between the summations is used when the two radial drives are in-phase, i.e., when both drives are directed outward, and the negative sign used when the drives are out-of-phase. Following the procedure given above for the single radial drive yields

$$\tilde{f}_3(k, \phi) = \frac{F}{(2\pi)^2 a} e^{-ikx_0} \left[\sum_{n=-\infty}^{\infty} e^{in(\phi - \phi_0)} \pm \sum_{n=-\infty}^{\infty} (-1)^n e^{-in(\phi - \phi_0)} \right] . \quad (36)$$

Comparing with Equation (5) yields

$$\tilde{f}_{3n}(k) = \frac{F}{(2\pi)^2 a} [1 \pm (-1)^n] e^{-i(kx_0 + n\phi_0)} . \quad (37)$$

Examination of this result reveals that for the in-phase case, only the even circumferential modes contribute to the solution, whereas for the out-of-phases case, only the odd modes contribute.

2.6.3 The Circumferential Moment Drive

As illustrated in Figure 2, the expression for the pressure for the circumferential moment drive at (x_0, ϕ_0) is found by starting with two out-of-phase radial point forces; one at (x_0, ϕ_0) and the other at $(x_0, \phi_0 - d\phi)$, so that

$$f_3(x, \phi) = F\delta(x - x_0) \left[\sum_{m=-\infty}^{\infty} \delta \{ a [\phi - (\phi_0 + 2\pi m)] \} - \sum_{m=-\infty}^{\infty} \delta \{ a [\phi - (\phi_0 - d\phi + 2\pi m)] \} \right] . \quad (38)$$

Applying the Fourier transform on x and Poisson's summation formula, Equation (38) reduces to

$$\tilde{f}_3(k, \phi) = \frac{-Fe^{-ikx_0}}{(2\pi)^2 a} \sum_{n=-\infty}^{\infty} [e^{in(\phi + d\phi - \phi_0)} - e^{in(\phi - \phi_0)}] . \quad (39)$$

Multiplying numerator and denominator by $ad\phi$ and taking the limit as $d\phi \rightarrow 0$, Equation (39) reduces to

$$\tilde{f}_3(k, \phi) = \frac{-Me^{-ikx_0}}{(2\pi a)^2} \frac{d}{d\phi} \sum_{n=-\infty}^{\infty} e^{in(\phi - \phi_0)} \quad (40)$$

where M is the magnitude of the applied moment $Fad\phi$. The final expression for the n^{th} circumferential mode is

$$\tilde{f}_{3n}(k) = \frac{-iMn}{(2\pi a)^2} e^{-i(kx_0 + n\phi_0)} . \quad (41)$$

2.6.4 The Axial Moment Drive

The expression for the axial moment drive at (x_0, ϕ_0) is obtained from two out-of-phase radial point forces; one at (x_0, ϕ_0) and the other at $(x_0 - dx, \phi_0)$, such that

$$f_3(x, \phi) = F[\delta(x - x_0) - \delta(x - (x_0 - dx))] \sum_{m=-\infty}^{\infty} \delta \{ a [\phi - (\phi_0 + 2\pi m)] \} . \quad (42)$$

Multiplying Equation (42) by dx/dx and taking the limit as $dx \rightarrow 0$ yields

$$f_3(x, \phi) = -M\delta_1(x - x_0) \sum_{m=-\infty}^{\infty} \delta\{a[\phi - (\phi_0 + 2\pi m)]\} , \quad (43)$$

where M is the magnitude of the driving moment Fdx and δ_1 is the first order Dirac delta function. Applying the Fourier transform and Poisson's summation formula to Equation (43) yields

$$\tilde{f}_3(k, \phi) = \frac{ikMe^{-ikx_0}}{(2\pi)^2 a} \sum_{n=-\infty}^{\infty} e^{in(\phi - \phi_0)} \quad (44)$$

which results in

$$\tilde{f}_{3n}(k) = \frac{ikM}{(2\pi)^2 a} e^{-i(kx_0 + n\phi_0)} . \quad (45)$$

2.6.5 The Circumferential In-Plane Drives

The circumferential in-plane drive is illustrated in Figure 3. The expression for the circumferential in-plane drives is similar to the expression derived for the double radial drive.

$$\tilde{f}_{2n}(k) = \frac{F}{(2\pi)^2 a} [1 \pm (-1)^n] e^{-i(kx_0 + n\phi_0)} . \quad (46)$$

where F is the magnitude of each one of the in-plane drives. The positive sign indicates the two drives are in-phase and the negative sign indicates that they are out-of-phase. As with the double radial drive, only even circumferential modes are excited by the in-phase drives and only odd modes are excited by the out-of-phase drives.

2.7 Acoustic Radiation

An expression for the acoustic pressure in the fluid medium can be derived from Equations (14) and (15)

$$\bar{p}^f(r, k, \phi) = i\rho_o\omega \sum_{n=-\infty}^{\infty} \frac{\tilde{w}_n(k) H_n^{(1)}[(k_o^2 - k^2)^{1/2} r] e^{in\phi}}{(k_o^2 - k^2)^{1/2} H_n^{(1)'}[(k_o^2 - k^2)^{1/2} a]} \quad (47)$$

where \tilde{w}_n is given by Equation (28) for the transverse drives and by Equation (30) for the circumferential in-plane drives. In the acoustic far field, $r \rightarrow \infty$, the Hankel function can be written as

$$H_n^{(1)}[(k_o^2 - k^2)^{1/2} r] \xrightarrow{r \rightarrow \infty} \left[\frac{2}{\pi(k_o^2 - k^2)^{1/2}} \right]^{1/2} \cdot e^{i[(k_o^2 - k^2)^{1/2} r - \frac{n\pi}{2} - \frac{\pi}{4}]} \quad (48)$$

Using this approximation in Equation (47), taking the inverse Fourier transform and applying the method of stationary phase, produces the following expression for the magnitude of the acoustic pressure at the observation point (R, θ, ϕ) in the surrounding medium:

$$|p^f| = \left| \frac{2\rho_o c_o}{R \sin\theta} \sum_{n=-\infty}^{\infty} \frac{\tilde{w}_n(k_o \cos\theta) e^{in\theta} (-1)^n}{H_n^{(1)'}(k_o a \sin\theta)} \right| \quad (49)$$

3.0 DESCRIPTION OF MEASUREMENTS

Before exercising the analytic model to explore the influence that the types of drives have on acoustic radiation from ribbed cylindrical shells, predictions are compared to measurements to assist in validating the model for investigation of acoustic radiation from ribbed cylindrical shells. It is not possible to experimentally duplicate an infinite ribbed cylindrical shell with uniformly spaced ribs. The shell used in the measurements is not completely modeled by the analytic model described above in Section 2. However, many of the major features of the shell used in the measurements are represented in the analytic model, so that comparisons of predicted and measured results can be used

to assist in the verification of the model for purposes of meeting our objective of determining the effects that different drives have on acoustic radiation from ribbed cylindrical shells and to identify some of the mechanisms of radiation from ribbed cylindrical shells.

3.1 The Shell

The shell used in the measurements was constructed of aluminum in five ribbed cylindrical sections which were bolted together at joint bands to make a twenty foot shell. Figure 4 is a sketch of one of the shell sections. As shown in Figure 4, the shell thickness was $5/16$ inches and the outer diameter 21 inches. Each section had five ribs, with heights of $1\ 1/16$ inches and widths of $3/8$ inches, spaced from 7 to 8 inches apart. The joint bands, which were $1\ 9/16$ inches high and $3\ 3/4$ inches wide, served as the second set of ribs shown in Figure 1. In addition to the ribs and joint bands, each shell section had two hand hole covers and two longitudinal rails. In the single radial and moment drives, the shakers were located in between the two longitudinal rails. The shell was sealed on the ends with flat $1\ 1/2$ inch thick steel end caps.

3.2 Shaker Configurations

There were seven types of drives treated in the analytic model (See Figures 2 and 3). Each of these drives was employed in the measurements. Only drives located in the middle of the middle shell section on a rib will be considered here. For the single and double radial drives, the shaker was mounted to $1\ 1/2$ by $1\ 1/2$ inch aluminum blocks, which had a heights of $2\ 3/8$ inches above the shell surface. The blocks were welded to the shell. For the moment drives, the shakers

were mounted to a bar which was bolted to the shaker mount block as shown in Figure 5 for the circumferential moment drive. For the axial moment drive, the moment drive bar was rotated 90°. For the longitudinal drives, the shakers were mounted to a bar which spanned across the diameter of the shell as shown in Figure 6. The ends of the bar were pinned to mounting blocks welded to the shell. All shakers were attached to the mounting via threaded studs.

3.3 Measurement Configuration and Instrumentation

During frequency sweeps from 20 to 5000 Hz, the radiated noise was measured by a hydrophone located at a distance of 45 feet from the centerline of the shell in a direction perpendicular to the shell axis opposite the middle of the shell. The shell was rotated about its axis so that the bottom of the shakers in the single radial, moment and longitudinal drives faced the hydrophone. In the double radial drive, the second shaker was located on the side of the shell opposite the hydrophone. The shell and hydrophone were located 245 feet below the surface in water 550 feet deep.

Each shaker had an impedance head, with a force gage and accelerometer that measured the force applied by the shaker to its attachment point and the acceleration at the attachment point. The shakers were driven by a swept frequency voltage signal from 20 to 5000 Hz. For the drives with two shakers, i.e., the double radial, moment and longitudinal drives, the shakers were driven with the same voltage signal. For the in-phase drives, the same voltage signal was input to both shakers. For the out-of-phase drives, i.e., the moment and out-of-phase longitudinal drives, the electrical leads to the second shaker

were reversed so that the voltage signal to the second shaker was 180° out-of-phase from the voltage signal to the first shaker.

3.4 Data Reduction

The sound pressure level of the noise radiated from the shell at the drive frequency, measured by the hydrophone, was compared to ambient noise levels measured prior to each radiated noise measurement. If the measured radiated noise level was less than 3 dB above the measured ambient noise level, the data were discarded. If the measured radiated noise level was 3 to 10 dB above the ambient noise level, the ambient noise was subtracted from the radiated noise. No correction was applied if the radiated noise level was above the ambient noise level by more than 10 dB. The ambient noise corrected radiated noise levels were corrected to a distance of 1 yard by subtracting $20 \log_{10} R$, where R is the measurement distance of 15 yards. The corrected sound pressure levels were normalized to the total input force or moment applied to the shell.

To estimate the force applied to the inside surface of the shell for the radial drives, the force required to accelerate the shaker mount block was subtracted from the force measured by the shaker force gage. The force required to accelerate the shaker mount block was computed as the product of the mass of the mount block and the acceleration measured by the shaker accelerometer. At some frequencies, this computed force was greater than the applied force. This usually occurred near resonances where the measured acceleration was largest. At these frequencies, the force applied to the shell could not be accurately determined so that the measured radiated noise levels could not be normalized for the force input to the shell. The data were discarded at

frequencies where the input force to the shell could not be determined for the radial drives. Data were also discarded for the double radial drives when the measured magnitudes of the forces for the two shakers differed by more than 3 dB.

For the moment drives, the moment applied to the shell was estimated using the following equation derived using free Bernoulli-Euler beam theory

$$M = \frac{2F}{k} \left[\frac{\sin(kl) + \sinh(kl)}{1 + \cos(kl) \cosh(kl)} \right] \quad (50)$$

where F is the measured shaker force, l is the distance from the shaker drive point to the center of the shaker moment drive bar and k is the free bending wavenumber in the bar at the drive frequency. At frequencies where the magnitudes of the forces measured by the two shaker force gages differed by more than 3 dB, the radiated noise data were discarded as resulting from other than a pure moment drive. For the in-phase longitudinal drives, the forces at the shell surface at the ends of the shaker mount bar were estimated from

$$F_s = F_m \left[\frac{\frac{(T-1)\cos kt}{1 + T \frac{\cos kt}{\cosh kt}} - \cosh kt}{\cosh kt (\cos kt \cos ka + \sin kt \sin ka)} \right] \quad (51)$$

where

$$T = \frac{\cosh kt \cosh ka - \sinh kt \sinh ka}{\cos kt \cos ka + \sin kt \sin ka} \quad (52)$$

and l is half the length of the shaker mount bar, a is the distance from the center of the shaker mount bar to the location of the shaker mount, F_m is the measured shaker force and F_s is the longitudinal force applied to the shell. For the out-of-phase circumferential drives

$$F_s = F_m \left[\frac{\frac{(T-1) \sinh kt}{1 + T \frac{\sinh kt}{\cosh kt}} - \sinh kt}{\sinh kt (\cosh kt \cos ka + \sinh kt \sin ka)} \right] \quad (53)$$

Equations (51) and (53) are derived using simply-supported Bernoulli-Euler beam theory. Radiated noise data were discarded at frequencies where the magnitudes of the shaker forces differed by more than 3 dB.

The measured data were limited by ambient noise at the low frequencies, typically below 200 Hz, where the ambient noise levels were highest and the radiated noise levels from the shell the lowest and at the high frequencies where the forces applied by the shakers in the two shaker drives were not equal in magnitude. Typically, above 1 kHz, the forces applied by the shakers driven with the same voltage signal, in or out of phase, were not of equal magnitude. Also, above 1 kHz, the equations used to estimate the forces or moments applied to the shell surface were not accurate. Therefore, measured radiated noise data are not presented for frequencies above 1 kHz.

4.0 VALIDATION OF ANALYTIC MODEL

First, the analytic model is validated by comparing predictions to published results for a large shell radius where the shell behaves like a flat plate and to measured results taken in the experiments described above in Section 3.0. Once validated, the analytic model is exercised in Section 5.0 to explore the dependence of acoustic radiation from fluid-loaded ribbed cylindrical shells on shell damping, ribs and radius, and type and location of drives.

4.1 Comparison to Published Results

As the radius increases, the response of and the acoustic radiation from the cylindrical shell should approach the response of and acoustic radiation from a flat infinite plate. Therefore, to check the validity of the shell model, results from Equation (49) for a large ($a = 100$ ft) shell radius are compared to results from published investigations on the acoustic radiation from flat infinite plates. In Figure 7, results for the acoustic radiation at 1 kHz as a function of observation direction (θ in Figure 1) for the unsupported shell driven by a single point radial drive and an axial moment drive are compared with results from Feit [30] for the acoustic radiation from an unsupported, flat, infinite plate driven by a force and a moment. For both the radial and moment drives, the agreement shown in Figure 7 is good, which helps to verify the shell model and the models used for the radial and moment drives. In Figures 8 and 9 acoustic radiation in a direction normal to a shell of large radius driven by a point radial drive are compared to results presented by Mace [16] for a flat infinite plate. In Figure 8, the comparison is made for the shell and plate with a single set of parallel periodic supports, whereas in Figure 9, the comparison is made for the shell and plate with two sets of parallel periodic supports. Both figures show good agreement between the shell and plate results.

4.2 Predictions versus Measurements

For a 5/16-inch thick aluminum plate in water the critical frequency is around 29 kHz, so that the critical frequency for the measurement shell should be much higher than the highest measurement frequency of 1 kHz. At frequencies below the critical frequency, three mechanisms of acoustic radiation from periodically ribbed cylindrical

shells excited by localized sounds are dominant. First, radiation is produced by the near field structural response around the localized drives. Second, scattering from the ribs produce areas of acoustic radiation, which act as an array of localized sources with the rib spacing. Third, radiation from resonant modes of the finite unbaffled shell occurs from the ends of the shell. Since the predictions are for an infinite shell, radiation at frequencies of resonance that appear in the measured radiated noise levels will not appear in the predicted radiated noise levels.

Since the radial drives were the easiest to generate in the measurements, comparison between predictions and measurements for the radial drives should provide the best test of validation of the analytic model that minimizes the test of our ability to generate the ideal drives assumed in the analytic models. In Figure 10, the predicted and measured radiated noise levels are compared for the single radial drive. There are several peaks in the measured levels associated with radiation at frequencies at the shell resonances. These peaks are incomplete peaks in the measured levels in Figure 10 because, at resonance, the force on the shell surface could not be determined from the measured shaker force so that the data around the frequencies of resonance were discarded. The only large peak where the measured data are complete occurs at 560 Hz. Peaks in the acoustic radiation for periodically ribbed structures occur when the free bending wavenumber is

$$k = \frac{2\pi n}{d} \quad (54)$$

where d is the spacing between the ribs and n is an integer.

Equation (54) can be interpreted as the main or aliasing beam in the acoustic radiation pattern from an array of sources at the rib locations where the radiation from the sources are in phase; i.e., when the phases of the waves in the structure are all equal at the rib locations, or when a resonance in the vibration between the ribs occurs in the structure. Using the free bending wavenumber for an unloaded 5/16-inch aluminum plate and a rib spacing of 7 1/2 inches, Equation (54) yields a frequency of 2.1 kHz for $n = 1$, which is outside the measurement frequency range in Figure 10. For $d = 46$ inches, the spacing between the joint bands, Equation (54) yields 56, 225, 507 and 901 Hz for $n = 1, 2, 3$ and 4 respectively. With fluid loading, these frequencies will be less. Frequencies of resonances for the measurement shell were reduced by almost one half when the shell was immersed in water [31]. This implies that the above frequencies for the peaks in the radiation due to scattering from the joint bands will be lower. Therefore, it is likely that the peaks that appear in the predicted radiated noise levels in Figure 10 below 700 Hz are due to wave scattering by the joint bands. The largest of these peaks occurs at 600 Hz. There is a corresponding peak in the measured levels at 560 Hz that is probably associated with scattering from the ribs and not resonances because there is no data dropout about this peak and no resonances were identified in the shell near 560 Hz [31]. The other two peaks due to rib scattering are too weak to be identified in the measured levels. In addition to the radiation due to rib scattering, agreement between the predicted and measured levels in Figure 10 is good at nonresonance frequencies. Since these levels are probably due largely to radiation from the structural near field of the source where the ribs and resonances are not factors,

agreement should be good at the nonresonance frequencies if the analytic model is valid. Agreement at nonresonance frequencies and in the peaks associated with rib scattering between the predicted and measured levels in Figure 10 indicates that the analytic model is faithfully representing the principle radiation mechanisms for a ribbed infinite cylindrical shell.

The predicted and measured radiated noise levels for the out-of-phase double radial drive are compared in Figure 11. There are three peaks in the predicted levels below 700 Hz. Because these peaks occur at the same frequencies as the peaks in the predicted levels for the single radial drive, they are probably associated with rib scattering. In the measured levels, the only complete peak with a level 10 dB above the background occurs at 655 Hz, above the frequency of 600 Hz for the peak in the predicted levels. For the single radial drive, the peaks in the measured levels occurred at a frequency below the frequency for the peak in the predicted levels, opposite from the results shown in Figure 11. This shift in the frequency in the measurements may be due to the increased stiffness around the hand hole covers that were on both sides of the second shaker. In Figure 12, predictions are compared to measurements for the in-phase double radial drive. Peaks do not occur in the predicted levels for radiation from the rib scattering. With in-phase radial drives located on opposite sides of the shell, the $n = 2$ circumferential bending modes will be excited, and the $n = 1$ circumferential rigid body modes will be suppressed. For circumferential mode numbers greater than one, the bending wavenumber that satisfies Equation (53) is higher than the $n = 1$ modes since the direction of propagation is no longer axial, but in the direction of a

spiral around the shell. Therefore, the peak in the radiation due to rib scattering will occur at higher frequencies out of the frequency range of the measurements. In Figure 12, a peak does occur in the measured levels around 600 Hz, which may be due to rib scattering. Because the forces produced by the two radial shakers were only within 3 dB, there could be a single radial drive component in the double drive that produced the peak shown in Figure 12 at 600 Hz. The peak in Figure 12 is 10 dB less than the peak for the single radial drive shown in Figure 10, so that adding the second in-phase drive reduced the peak by 10 dB. In the predictions, where perfect in-phase drives are assumed, the peak is completely eliminated when the second in-phase drive is added.

Outside of the resonant peaks and peaks due to rib scattering, the predicted and measured radiated noise levels in Figure 11 and 12 are in good agreement. The decrease in the levels for the in-plane double radial drive in Figure 12 at frequencies below 300 Hz occurs in both the measurements and predictions. This is probably due to the interference between the two sources which are exerting forces on the shell in opposite directions (see Figure 2). At low frequencies, these forces excite the $n = 0$ circumferential breathing mode, which has a much higher impedance than the other circumferential modes that are excited at higher frequencies.

In general, the agreement between the predicted and measured radiated noise levels for the radial drives is sufficient to validate the analytic model for our purposes of exploring the influence the ribs and different types of drives have on the acoustic radiation from ribbed cylindrical shells.

The measured and predicted radiated noise levels for the axial moment drive are compared in Figure 13. There are fewer measured data shown for the moment drive than for the radial drives. The measured shaker forces interacted more in the moment than the radial drives which resulted in more data being discarded because the measured shaker forces were not equal in magnitude. Agreement between the predicted and measured levels in Figure 13 is not as favorable as the agreement achieved with the radial drives. The predicted levels are lower than the measured levels at all frequencies except the highest frequencies for which measured levels are available. In the analytic model, a point moment drive is assumed where the separation between the two point drives that form the moment is infinitesimal, as shown in Equation (42). As the separation distance decreases, the imaginary part of the moment impedance increases [32]. This means that more of the energy imparted to the shell goes into the structural near field which, for moment drives, is a poor acoustic radiator. Therefore, in the analytic model with the ideal point moment drive, the radiation per unit moment drive is lower than in the measurements where the separation of the drives at the shell surface was approximately one inch, far from infinitesimal, so that more of the input energy went into propagating waves which radiate during scattering from ribs. As frequency and therefore ka where k is the free bending wavenumber and one-half the separation distance between the moment drives increases, the predicted and measured levels in Figure 13 come together.

In Figure 14, the predicted and measured levels for the circumferential moment drive are compared. The predicted levels are higher for the circumferential moment drive than for the axial moment

drive because the curvature in the circumferential direction increases the phase speed for waves generated in the circumferential direction by the circumferential moment drive which increases the radiation efficiency. The sparsity of measured data in Figures 13 and 14 make it difficult to see this increase in the radiation at nonresonance frequencies.

Predicted and measured levels for the in-plane circumferential drives are compared in Figures 15 and 16. In the measurements, it was impossible to generate pure in-plane circumferential drives. In the analytic model, pure in-plane circumferential drives were easy to simulate. The differences in the measured and predicted levels are probably more representative of the failure to produce in-plane circumferential drives with the shaker configuration shown in Figure 6 than the failure to model the response of and radiation from the shell.

5.0 NUMERICAL RESULTS

Numerical results given below are far field sound pressure levels referenced to 1 μ Pa pressure and corrected to a distance of 1 meter. For the single radial, double radial, and circumferential in-plane drives, the levels are normalized to 1 pound applied force. For the axial moment and circumferential moment drives, the levels are normalized to 1 foot-pound. Unless otherwise noted, the parameters given in Table 1 are used. With the exception of the hand-hole covers and longitudinal rails, the parameters in Table 1 model the shell used in the measurements.

In Figures 17 through 20, the effect of internal structural damping on the acoustic radiation from the shell with two sets of ring supports

is examined for four types of drives: single radial, out-of-phase double radial, circumferential moment, and out-of-phase and in-phase double circumferential. Damping is modeled by use of a complex elastic modulus $E(1 - i\eta)$, where η is the loss factor. Results are compared for two values of the loss factor; 0.0 for no internal damping and 0.1 for heavy internal damping. As the results in Figures 17 through 19 show, increasing the damping reduces both the peaks and valleys in the acoustic radiation for the radial and moment drives at frequencies above 1500 Hz. Because the energy propagating from the source location is dissipated in the damped shell, the number of ring supports that are reached by propagating waves in the damped shell is reduced. This reduces the effective number of acoustic ring radiators that contribute to the peaks and valleys in the acoustic radiation. The results in Figures 17 through 19 show that at frequencies below 1500 Hz, damping has little effect on the mean value of the acoustic radiation where peaks and valleys do not occur. The radiation at these frequencies is largely controlled by the high wavenumbers in the structural near field of the point drives. Since the near field is composed largely of forced waves, damping has little effect in the near field of the structural source and consequently on the resulting acoustic radiation. Damping has the same effect for all of the radial and moment drives considered here, which also suggests that damping has little or no effect on the shell response near source locations.

At frequencies above 1500 Hz, the radiation from the damped shell is lower than the minimum radiation from the undamped shell. The damped radiation curve falls below the valleys in the undamped radiation curve instead of between the peaks and valleys as it does at frequencies below

1500 Hz. The damped curve is similar to the radiation curve for the unribbed shell, presented later in this paper (see Figure 21). This implies that the damping removes the effect of the ribs on the radiation by damping the vibration propagation from the drive point to the nearest rib. At higher frequencies, where the number of wavelengths between ribs will increase, the attenuation due to damping will increase, reducing the vibration levels at the ribs close to the drive point.

In Figure 20, the effect of damping on the acoustic radiation from circumferential in-plane drives is presented. A peak in the radiation occurs near one-half the ring frequency of the shell (approximately 3.5 kHz). As will be seen later, when the drives are out of the phase, the in-plane circumferential drives generate a breathing mode of vibration in the shell that produces acoustic radiation that is not sensitive to the ribs. Because the response to this excitation is dissipated by the shell damping, the radiation is reduced. Near the ring frequency of 3.5 kHz, the coherent effect of the two out-of-phase drives is reduced so that the response at the ring frequency is increased producing higher radiation levels, as shown in Figure 20.

Results for the acoustic radiation from the shell with both sets of ribs, with one set of ribs and with no ribs, are compared in Figures 21 through 23 for different drive types. The results in Figures 21 through 23 for the radial and circumferential moment drive show no peaks in the acoustic radiation for the unsupported cylinder. Since the results are for frequencies well below the critical frequency (~ 29 kHz), acoustic radiation is mostly from the structural near field of the driving force. For the supported cylinder, peaks occur in the acoustic radiation at frequencies below the critical frequency. With only the first set of

ribs the first peak in the acoustic radiation occurs around 1750 Hz. However, with the cylinder stiffened by both set of ribs, peaks occur at frequencies as low as 600 Hz because the second set of ribs are more widely spaced than the first set. Since the primary source for these peaks in the acoustic radiation is wavenumber scattering at the shell/rib junctions where non-radiating wavenumbers above the acoustic wavenumber are converted into radiating wavenumbers below the acoustic wavenumber, the cylinder appears as an array of equally-spaced ring radiators. The peaks in the acoustic radiation can then be attributed to the coherent addition of the radiated acoustic energy from an array of ring radiators on the shell surface. At an observation point perpendicular to this array ($\theta = 90.0$ degrees in Figures 21 through 25), aliasing peaks in the acoustic radiation pattern should occur near frequencies where

$$k_{fb} = \pm M \frac{2\pi}{L} \quad (55)$$

where M is an integer, k_{fb} is the free bending wavenumber of the shell, and L is equal to the ring spacing of either the first set of rings d , or the second set of rings D . For the cylinder with only the first set of rings, Equation (55) predicts that the first aliasing peak occurs at 1665 Hz, which is close to 1750 Hz where a peak occurs in the predicted results for the radial and circumferential moment drives. With the second set of ribs, the L in Equation (55) is larger, so that the equation is satisfied at lower frequencies, as evidenced in Figures 21 through 23. With Equation (55) only five additional peaks should occur with every sixth rib in the first set a member of the second set of ribs. However, more than six peaks occur below 1750 Hz in Figures 21

through 23 and these peaks sometimes occur at different frequencies for different types of drives. The additional peaks are probably due to spiraling modes in the shell that are not accounted for in Equation (55). The second radial drive in Figure 22 may remove some of the modes in the shell, and thereby remove some of the peaks in the radiation seen with the single radial drive in Figure 21. Because the circumferential moment drive excites a different set of modes, not all of the peaks seen in the radiation for the single radial drive in Figure 21 appear in the radiation from the shell with the double set of ribs for the circumferential moment drive.

Unlike the other drives, the response of the shell to the axial moment drive is not symmetric in the axial direction. The axial moment drive is a dipole source with its axis in the axial direction so that most of the bending wave energy propagates in the axial direction. Since the left going bending waves are out-of-phase with the right going waves, the shell response is not symmetric with respect to the drive location. For the axial moment drive, the acoustic radiation levels for the unsupported shell and the shell supported by one set of ribs are much lower than the levels for the shell supported by both sets of ribs. Since the bending waves propagating in opposite directions from the axial moment source are out-of-phase, the acoustic radiation from the left part of the shell arrives at the observation point located normal to the shell out-of-phase with the acoustic radiation from the right part of the shell when the shell is either unsupported or supported only by the first set of ribs. However, with both sets of ribs, the second set is not symmetric about the drive location [see Table 1] so that cancellation of the symmetrically located, out-of-phase acoustic

radiation does not occur. Moving the observation location off of the normal removes the out-of-phase cancellation of the acoustic radiation from the unsupported shell and the shell supported by one set of ribs as shown in Figure 24. In Figure 25, results are compared for the acoustic radiation from the shell driven at two different axial locations; one that is not symmetrically located with respect to the second set of rings ($x_0 = 2d$) and the other that is located symmetrically with respect to the second set of rings ($x_0 = 3d$, as shown in Figure 1). When the drive location is moved to a location that is symmetric with respect to the second set of rings, then the cancellation at an observation location normal to the shell of out-of-phase acoustic waves from opposite parts of the shell containing both sets of ribs does occur as shown in Figure 25.

For the case of the in-plane drives (Figures 26 and 27), it can be seen that there is little differences in the acoustic radiation from the shell with or without the ring supports. For the in-phase drives, the acoustic radiation appears to reach an upper limit associated with the ring frequency of the shell (3.5 kHz), while for the out-of-phase drives, the peak occurs at 1.8 kHz, which is half the ring frequency. The two in-phase drives are both in phase with the circumferential shell motion of the ring mode of the shell. When the circumferential drives are out of phase, then both drives are in phase with the circumferential mode of the shell at twice the wavelength of the shell ring mode so that the peak in the shell motion (and radiation) occurs near one half the ring frequency. When the circumferential modes are excited, most of the shell motion is circumferential where the phase speed in the ribs and shell are equal. Therefore the ribs have nearly the same resonant

circumferential modes as the shell. This sympathetic circumferential motion between the shell and ribs reduces the effect of the ribs on modifying the shell motion and thereby the effect the ribs have on the acoustic radiation from the shell excited with circumferential drives.

In Figure 27, results for the out-of-phase drive show a peak in the acoustic radiation at 200 Hz for the shell with both sets of rings. For the in-phase drive, a peak occurs at 650 Hz for the shell with both sets of rings. These peaks do not occur for the unsupported shell or the shell with one set of ribs, which indicates that at these frequencies energy is getting transformed from longitudinal wavenumbers to bending wavenumbers that react with the ribs. These peaks do not occur at the same frequencies as the peaks in the acoustic radiation for radial drives because the mixture of longitudinal and bending wave energy is different for the circumferential in-plane and radial drives such that energy propagation speeds and consequently frequencies at which the peaks in the radiation occur will differ.

In Figure 28, results are presented for a 180 degree spatial sweep in polar angle at 890 Hz where a peak in the acoustic radiation occurs for drives located at one of the first set of ribs that is $2d$ from the nearest rib in the second set on one side and $4d$ from the nearest rib in the second set on the other side. A damping loss factor of $\eta = 0.01$ was used for these predictions. The ribs in the first set are symmetric with respect to the drive location but the ribs of the second set are not symmetric with respect to the drive location. When the shell has only one set of ribs, Figure 28 shows the expected symmetry in the acoustic radiation. However, when the second set of ribs is added, symmetry does not occur. This indicates that scattering by the ribs and

not resonances in the shell sections between the ribs is controlling the acoustic radiation since the shell is not being driven at a point that is symmetric with respect to the locations of the second set of ribs. Figure 29 shows that non-symmetric acoustic radiation patterns occur for both the single radial and moment drives when the drive location is not symmetric with respect to the second set of ribs. For the in-plane, out-of-phase circumferential drive, Figure 30 shows that the main lobe in the radiation pattern near $\theta = 90^\circ$ is symmetric with and without the second set of ribs, but the second set of ribs do add non-symmetry to the side lobes. At $\theta = 90^\circ$ the acoustic radiation is controlled by the source structural near field, and not by the rib/shell interaction. However, near $\theta = 45^\circ$, the scattering from the second set of ribs plays a significant role.

It was noted earlier that several peaks appeared in the radiation from the shell with the double set of ribs below the first peak in the radiation from the shell with only the first set of ribs. The fact that there are more than five of these peaks was attributed to the interaction of the ribs with spiraling modes in the shell. In Figure 31, the radiation from the shell with the double set of ribs excited by the circumferential moment is presented for different shell radii. As the radius of the shell is increased, the frequencies at which the peaks in the radiation occur decrease. With a larger shell radius, the path lengths for spiraling modes increase, which results in lower frequencies for each mode so that the frequencies of the radiation peaks also decrease with increasing shell radius, as shown in Figure 31. The same trend also occurred for the radial drives.

In Figure 32, the acoustic radiation from the shell with only the first set of ribs is displayed for four drive types: single radial, in- and out-of-phase double radial, and circumferential moment drives. Since the acoustic radiation data for the moment drives are normalized to 1 ft-lb and the data for the radial and in-plane drives normalized to 1 pound, comparisons can be made only between the relative levels of the acoustic radiation for these two types of drives. For all radial drives, a peak in the radiation occurs at 1750 Hz, which is the first aliasing peak for radiation from the ribs predicted by Equation (55). Below 1750 Hz, small peaks in the radiation occur for all drives. These peaks are due to resonances in the circumferential shell modes. The single radial drives excites all circumferential modes, the out-of-phase double radial drive only the odd-numbered modes, and the in-phase double radial drive only the even-numbered modes. Figure 32 also indicates that, when the observation point is located normal to the shell axis and facing one of the radial drive locations, the radiation from the shell per pound input force with only one set of ring supports is greatest with the single radial drive than either of the two double radial drives at frequencies below the first rib-aliasing frequency.

Comparisons of the acoustic radiation from the shell with both sets of ribs for different types of drives are made in Figure 33 through 35 to the acoustic radiation from the single radial drive. In Figure 33, the acoustic radiation for the single radial drive is compared to the acoustic radiation for the double radial drives. As in the case with the acoustic radiation from the shell with the first set of ribs, the single radial drive appears to be the more efficient radiator. The double in-phase radial drive again produces the lowest radiation levels

of the radial point drives. For the single and double out-of-phase radial drives, a strong peak occurs near 600 Hz, which is not present for the double in-phase radial drive. More peaks appear in the radiation for the single radial drive than in the radiation for the double radial drives. The double radial drives suppress half of the circumferential modes and thereby half of the spiraling modes of propagation that interact with the second set of ribs to produce peaks in the radiation at frequencies below 1750 Hz.

In Figure 34, the single radial drive is compared with both the axial moment and circumferential moment drives. Because of the differences in normalization factors for the radial and moment drives, only the shapes of the curves, and not the absolute levels, are meaningful. For the circumferential moment drive the radiation efficiency increases faster as the frequency increases than the radiation efficiency for the axial moment or radial drives. More peaks appear at frequencies below 1000 Hz for the axial moment drive, suggesting that this drive is more efficient in producing bending wave propagation in the shell in the axial direction than the other drives. Since it is propagation in the axial direction that interacts with the ribs, the rib/shell interaction produces peaks in the radiation for the axial moment drive at lower frequencies and with higher levels than the peaks for the other drives.

Figure 35 compares results for the single radial drive to results for the in-plane circumferential drives. At frequencies below 1500 Hz, both of the in-plane drives are poor radiators when compared to the single radial drive. The out-of-phase circumferential drive does not surpass the radial drive until near 1700 Hz and the in-phase

circumferential drive until near the ring frequency of 3.5 kHz. The in-plane drives are less efficient than the radial drive at low frequencies because the in-plane drives do not couple as well to the radial motion of the shell as do the radial drives. When the frequencies for circumferential in-plane modes are reached, more energy is transformed into the shell increasing the energy in the shell which may couple into the bending waves which increases the acoustic radiation levels.

6.0 CONCLUSIONS

For six different driving mechanisms, equations are derived for the farfield acoustic radiation from a fluid-loaded infinite circular cylinder stiffened by two sets of parallel, periodic rib supports. This model includes the effects of each of the two sets of rings in separate terms that are added to the expression for the acoustic radiation from the unsupported circular cylinder. The effect of internal structural damping is included in the model.

The model is validated by comparing predictions to published results and measurements presented in this paper. Published results for the acoustic radiation from an infinite flat plate are compared to predictions for the cylindrical shell with a large radius. Measurements taken on a finite, ribbed, cylindrical shell are compared to predictions for the infinite shell. In areas where the comparisons are known to be valid, the agreement is sufficient to validate the model for purposes of using the model to investigate the influence that ribs and different types of drives have on the acoustic radiation from cylindrical shells.

Numerical results for the acoustic radiation are presented with and without internal damping, with and without the ring supports, and for different types of mechanical drives.

The numerical results show that structural damping reduces both the peaks and valleys in the acoustic radiation for all drive types. Two mechanisms of acoustic radiation were identified: (1) radiation from low wavenumbers in the structural near field of the driving forces and (2) coherent addition of radiation associated with scattering by the ribs of high non-radiating to low radiating wavenumbers. Peaking in the acoustic radiation levels occurs at bending wavenumbers where aliasing of the array of rib radiators occurs and at frequencies where circumferential resonances in the rib supported shell occur.

The single radial drive produces greater acoustic radiation per pound of input force than the double radial drives. The in-plane circumferential drives are less efficient than the radial drives at producing acoustic radiation at frequencies below the first circumferential in-plane mode of the shell. At and above this mode, the circumferential in-plane drives produce greater radiation per pound of input force than the radial drives. The axial moment drive is more efficient at generating acoustic radiation from a ribbed cylindrical shell than the circumferential moment drive. However, at observation locations normal to the shell axis, the radiation efficiency of the axial moment drive is low when the drive is located symmetrically with respect to rib locations.

Although several types of drives are treated in this paper, all of the drives are applied at points on the shell middle surface. Distributed sources, such as single sources applied over finite areas or

pressure fluctuations in turbulent boundary layers applied over the entire shell surface, could be added to the model presented in this paper by integrating the results given in this paper for point drives over a given source distribution. Because it was assumed that the rib supports interact with the shell only through normal forces, scattering by the ribs of longitudinal waves into bending waves and scattering associated with moment reactions of the ribs are not included. Including shear force and moment reactions of the ribs would change the scattering of in-shell waves by the ribs and thereby change the acoustic radiation efficiency. Also, the rib/shell interaction was assumed to occur along the circular line of the intersection of the shell and rib. This produced wavenumber scattering into all wavenumbers. Making the intersection of the shell and rib finite in width would reduce the higher wavenumber scattering, which would affect the acoustic radiation efficiency.

REFERENCES

- [1] Maidanik, Gideon, "Response of Ribbed Panels to Reverberant Acoustic Fields," J. Acoust. Soc. Am., 34(6) pp. 809-826 (June 1962).
- [2] Lyon, Richard H., "Sound Radiation from a Beam Attached to a Plate," J. Acoust. Soc. Am., 34(9) pp. 1265-1268 (September 1962).
- [3] Nayak, P. Ranganath, "Line Admittance of Infinite Isotropic Fluid-Loaded Plates," J. Acoust Soc. Am., 47(1) pp. 191-201 (1970).
- [4] Maidanik, G., "Surface-Impedance Nonuniformities as Wave-Vector Convertors," J. Acoust. Soc. Am., 46(5) pp. 1062-1073 (1969).
- [5] Belinskii, B. P., "Radiation of Sound by a Plate Reinforced with a Projecting Beam," Sov. Phys. Acoust. 24(3) pp. 183-187 (May-June 1978).
- [6] Crighton, D. G. and G. Maidanik, "Acoustic and Vibration Fields Generated by Ribs on a Fluid-Loaded Panel, I: Plane-Wave Problems for a Single Rib," J. Sound. Vibr. 75(3) pp. 437-452 (1981).

- [7] Evseev, V. N. and V Yu Kirpichnikov, "Influence of the Wave Properties of a Reinforcing Beam on the Radiation from an Infinite Plate Driven by a Force Parallel to the Beam," Sov. Phys. Acoust. 23(5) pp. 393-396 (September - October 1976).
- [8] Lin, F., Gau, F. and Sabih I. Hayek, "Acoustic Radiation from Point Excited Rib-Reinforced Plate," J. Acoust. Soc. Am. 62(1) pp. 72-83 (July 1977).
- [9] Romanov, V. N., "Sound Radiation by an Infinite Plate with Reinforcing Beam," Sov. Phys. Acoust. 18(4) pp. 490-493 (April - June 1973).
- [10] Soyatenko, V. A., "Low-Frequency Radiation from a Beam-Reinforced Plate Driven by Distributed Forces," Sov. Phys. Acoust. 33(1), pp. 97-98 (January - February 1987).
- [11] Garrellick, Joel M. and Gau-Feng Lin, "Effect of the Number of Frames on the Sound Radiation by Fluid-Loaded, Frame-Stiffened Plates," J. Acoust. Soc. Am., 58(2) pp. 499-500 Letter to the Editor (1975).
- [12] Romanov, V. N., "Sound Radiation from an Infinite Plate Reinforced with a Finite Set of Beams and Driven by a Point Force," Sov. Phys. Acoust. 23(1) pp. 63-68 (January-February 1977).
- [13] Romanov, V. N., "Radiation of Sound by an Infinite Plate with the Reinforcing Beams," Sov. Phys. Acoust., 17(1) pp. 92-96 (July-September 1971).
- [14] Evseev, V. N., "Sound Radiation from an Infinite Plate with Periodic Inhomogenetics," Sov. Phys. Acoust 19(3), pp. 226-229 (November-December 1973).
- [15] Mace, B. R., "Sound Radiation from a Plate Reinforced by Two Sets of Parallel Stiffeners," J. Sound. Vibr. 71(3) pp. 435-447 (1980).
- [16] Mace, B. R., "Sound Radiation from Fluid Loaded Orthogonally Stiffened Plates," J. Sound. Vibr. 79(3) pp. 439-452 (1981).
- [17] Mead, D. J. and A. K. Mallik, "An Approximate Theory for the Sound Radiated from a Periodic Line-Supported Plate," J. Sound. Vibr. 61(3) pp. 315-326 (1978).
- [18] Plakhov, D. D., "Sound Field of a Multispan Plate," Sov. Phys. Acoust. 13(4) pp. 506-510 (April-June 1968).
- [19] Vyalyshev, I. and B. D. Tartakovskii, "Compensation of the Radiation from a Flexurally Vibrating Beam-Reinforced Plate," Sov. Phys. Acoust. 22(6) pp. 471-474 (November-December 1976).
- [20] Bernblit, M. V., "Sound Radiation by a Thin Elastic Cylindrical Shell with Reinforcing Ribs," Sov. Phys. Acoust. 20(5) pp. 414-418 (1975).

- [21] Bernblit, M. V., "Sound Radiation from a Ribbed Cylindrical Shell," Sov. Phys. Acoust. 21(6) pp. 518-521 (1976).
- [22] Ivanov, V. S. and V. N. Romanov, "Wideband Sound Radiation by Thin Beam-Supported Plates and Shells," Sov. Phys. Acoust. 24(3) pp. 198-202 (May-June 1978).
- [23] Lawrie, J. B., "An Infinite, Elastic, Cylindrical Shell with a Finite Number of Ring Constraints," J. Sound Vibra. 130(2) pp. 189-206 (1989).
- [24] El-Raheb, M. and P. Wagner, "Acoustic Radiation from a Shell with Internal Structures," J. Acoust. Soc. Am., 85(6) pp. 2452-2464 (June 1989).
- [25] Fuller, C. R., "Radiation of Sound from an Infinite Cylindrical Elastic Shell Excited by an Internal Monopole Source," J. Sound Vibr. 109(2), pp. 259-276 (1986).
- [26] Reddy, E. S. and A. K. Mallik, "Response of and Sound Radiation from a Layered Cylinder with Regular Axial Stiffness," J. Sound Vibr 103(4), pp. 519-531 (1985).
- [27] Burroughs, C. B., "Acoustic Radiation from Fluid-Loaded Infinite Circular Cylinders with Doubly Periodic Ring Supports," J. Acoust. Soc. Am. 75(3) pp. 715-721 (1984).
- [28] Thompson Jr., William and J. V. Ruttayya, "Acoustic Power Radiated by an Infinite Plate Excited by a Concentrated Moment," J. Acoust. Soc. Am. 36(8) pp. 1488-1490 (August 1964).
- [29] Feit, D., "Pressure Radiated by a Point-Excited Plate," J. Acoustic Soc. Am. 40(6) pp. 1489-1494 (1966).
- [30] Kennard, E. H., "The New Approach to Shell Theory: Circular Cylinders," J. Appl. Mech. 20 pp. 33-40 (1953).
- [31] Burroughs, C. B., Hayek, S. I., Bostian, D. A., and J. E. Hollander, "Resonant Frequencies and Mode Shapes for Single and Double Cylindrical Shells," ARL TM 83-169, 23 September 1983.
- [32] Cremer, L., Heckl, M., and E. E. Lingar, "Structure-Borne Sound," Springer-Verlog, New York, NY, Second Edition, pp. 311-315.

Table 1. Parameters Used in Shell Model

Shell Thickness - $h = 0.794$ cm

Shell Radius - $a = 2.67$ cm

Young's modulus for shell and ribs - $E = 6.9 \times 10^{11}$ dynes/cm²
(Aluminum)

Material Density for shell and ribs - $p = 2.56$ gm/cm³ (Aluminum)

For first set of ribs - width - $w_r = 0.95$ cm
height - $h_r = 2.71$ cm

For second set of ribs - width - $w_r = 6.35$ cm
height - $h_r = 2.71$ cm

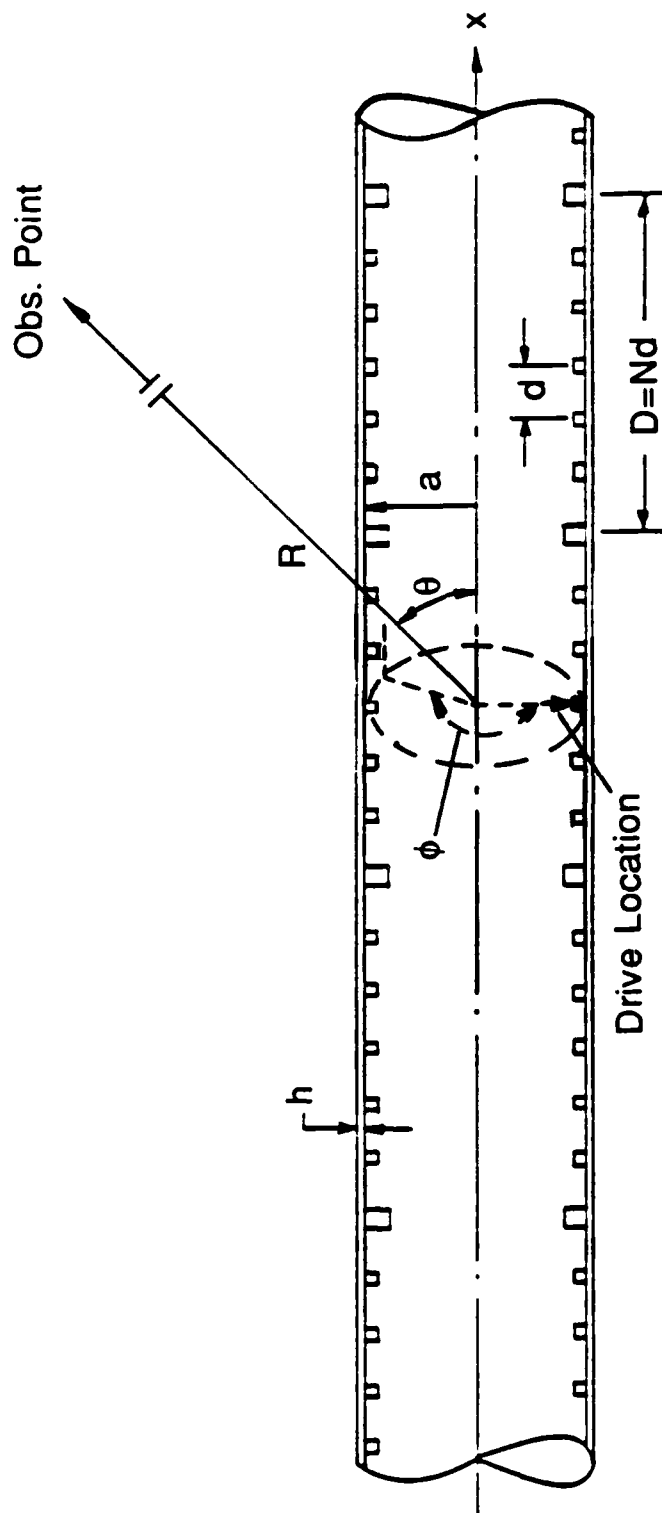
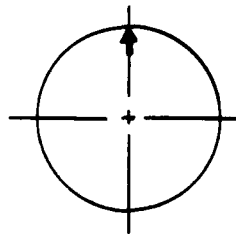
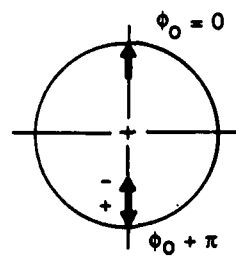


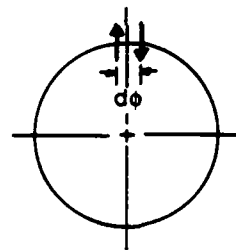
Figure 1. Geometry and Coordinate System for Doubly Periodic Ribbed Cylindrical Shell



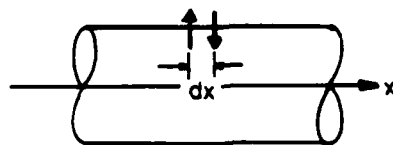
Single Radial Drive



In (+) and out (-) of Phase Double Radial Drive

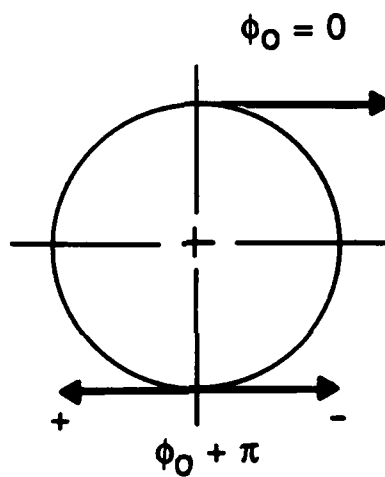


Circumferential Moment Drive



Axial Moment Drive

Figure 2. Radial and Moment Drives



In (+) and Out (-) Of Phase In-Plane Circumferential Drive

Figure 3. In-Plane Circumferential Drives

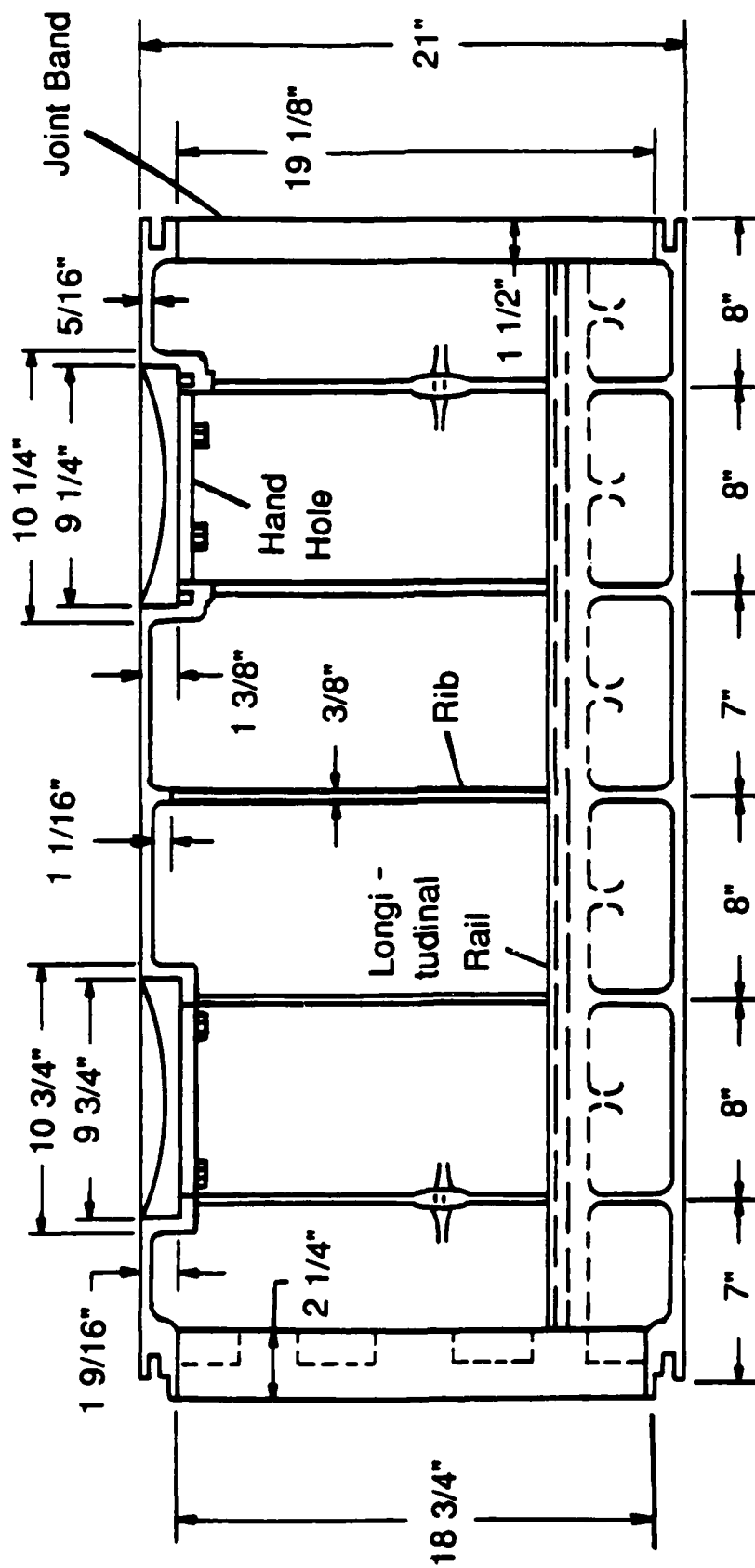


Figure 4. Section of Shell Used in Measurements

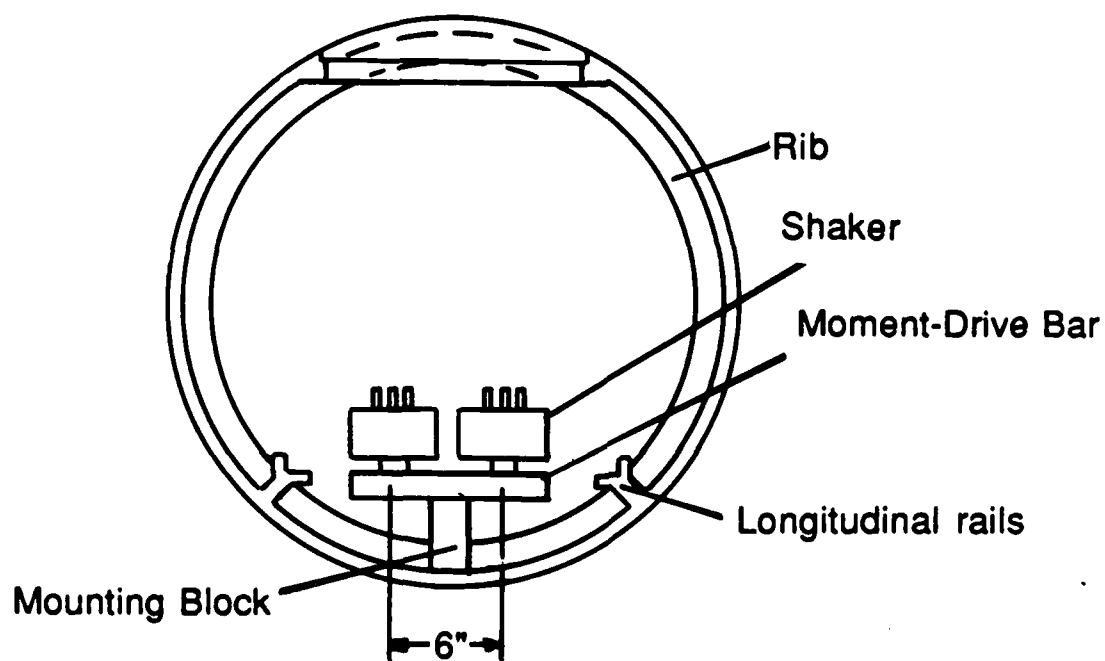


Figure 5. Shaker Mounting Arrangement for Circumferential Moment Drive

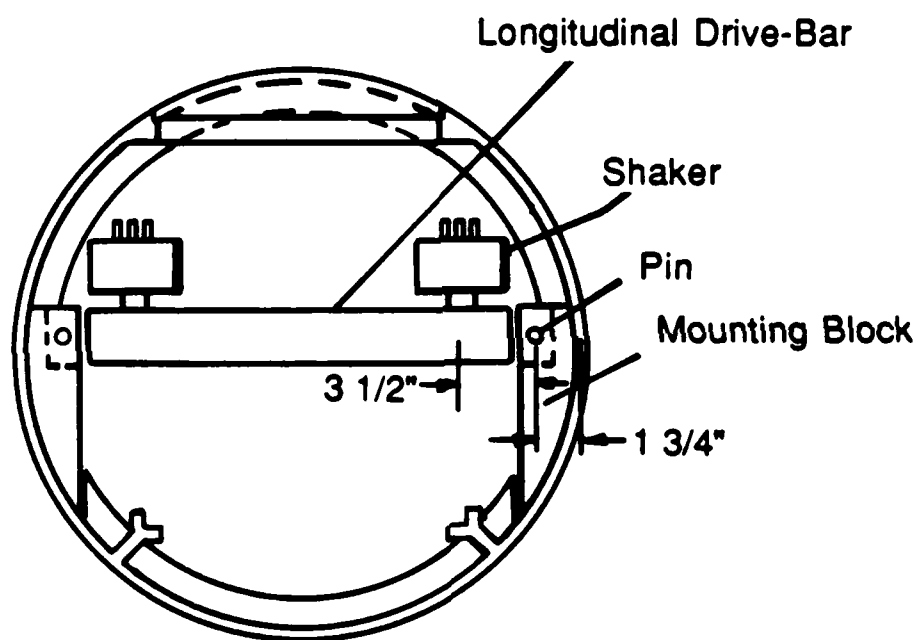


Figure 6. Shaker Mounting Arrangement for Longitudinal In-Plane Drives

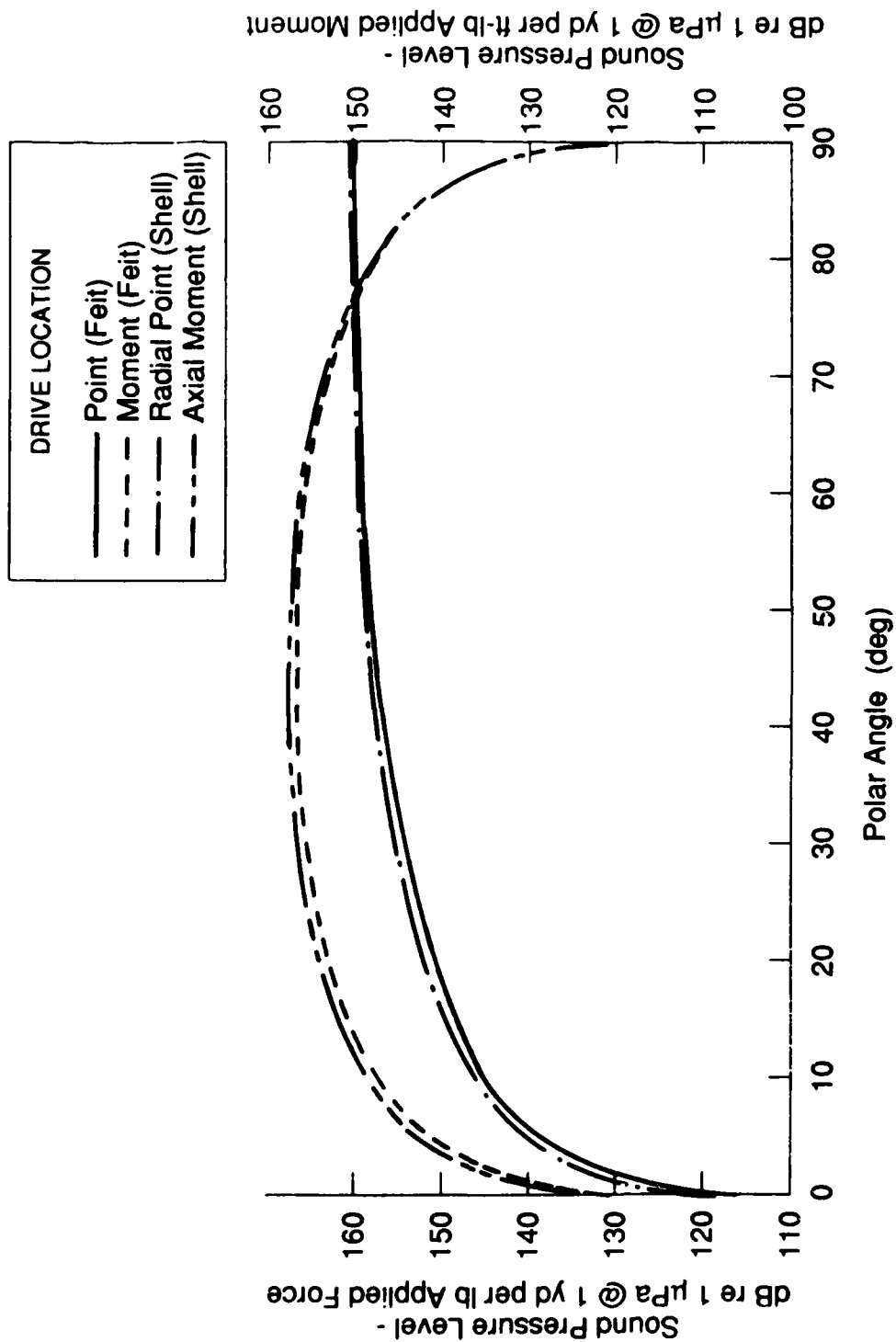


Figure 7. Comparisons of Predictions of Acoustic Radiation from an Unsupported Cylindrical Shell with a Large Radius to Published Predictions for an Unsupported Flat Plate

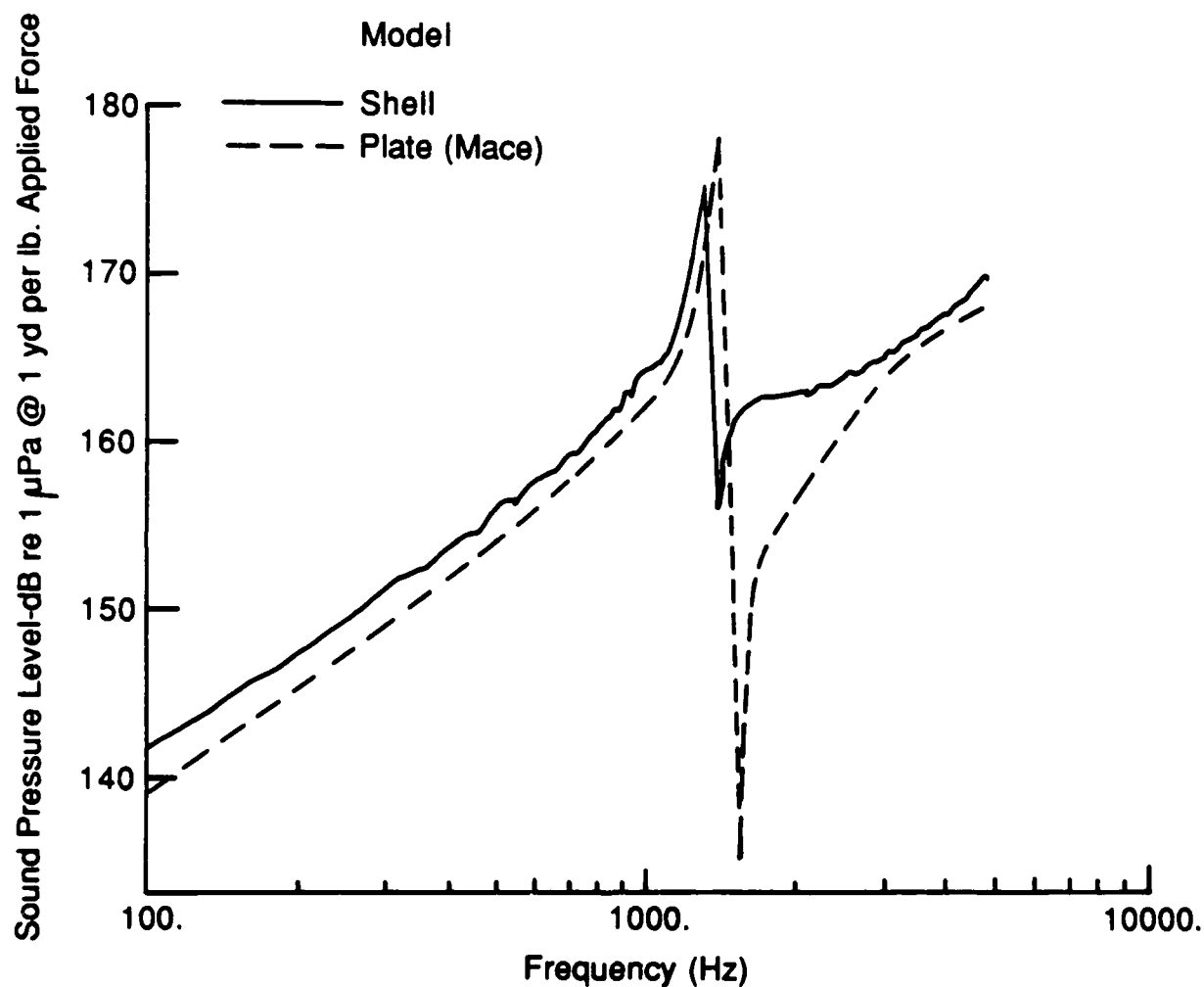


Figure 8. Comparison of Predictions of Acoustic Radiation from a Cylindrical Shell with Single Periodic Ribs and Large Radius to Published Predictions for Flat Plate with Single Periodic Line Supports

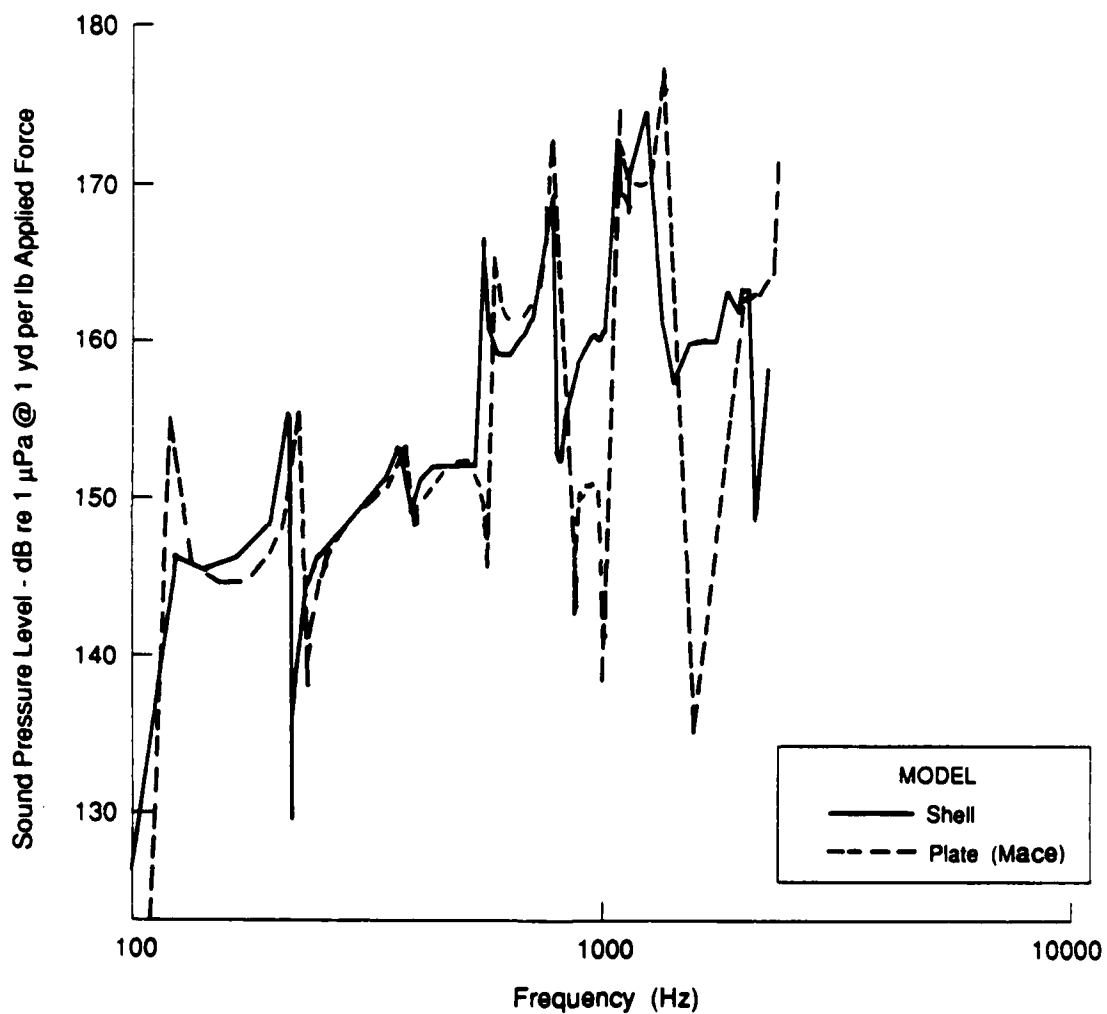


Figure 9. Comparison of Predictions of Acoustic Radiation from a Cylindrical Shell with Doubly Periodic Ribs and Large Radius to Published Predictions for Flat Plate with Doubly Periodic Line Supports

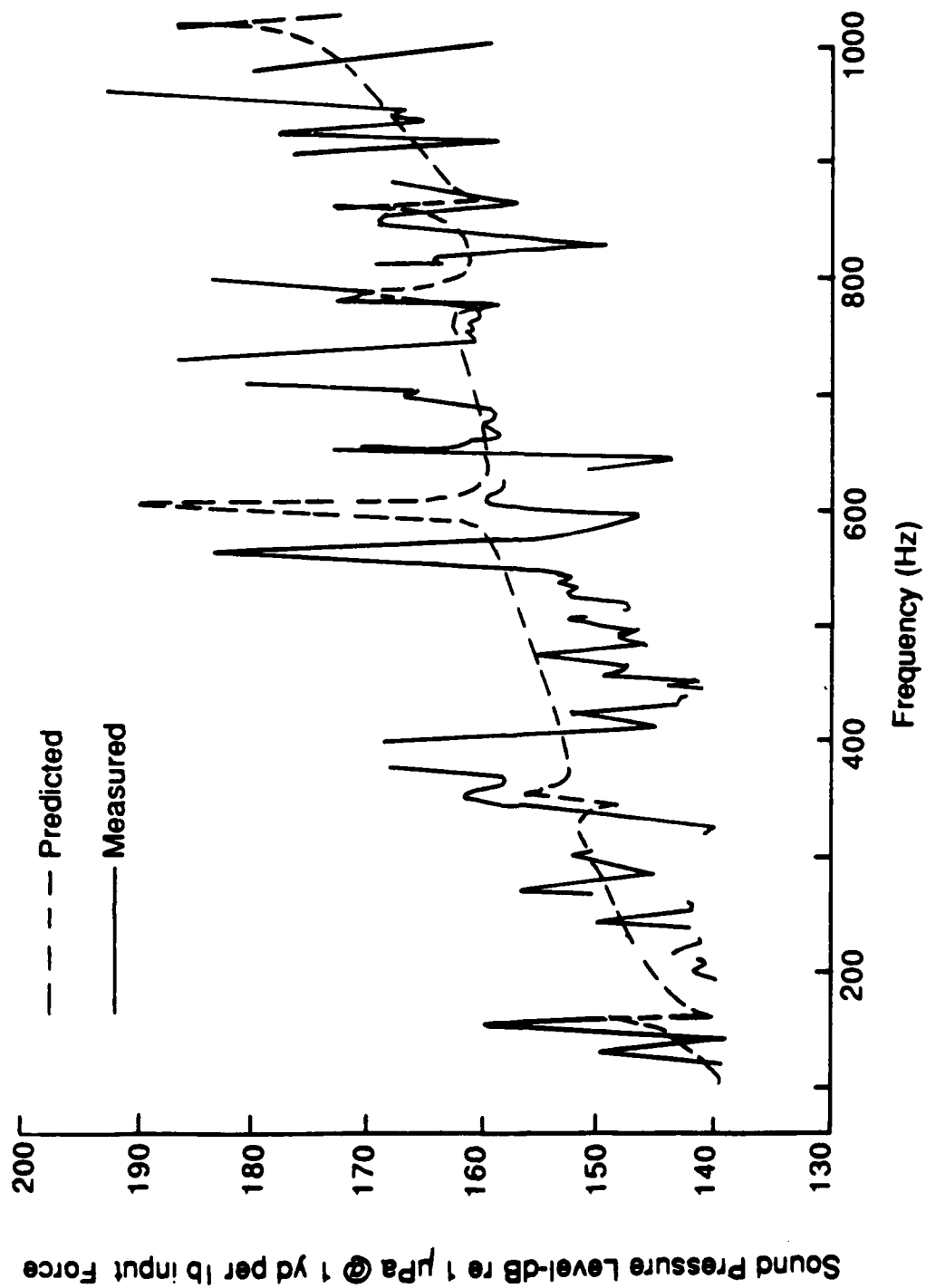


Figure 10. Comparison of Predicted and Measured Acoustic Radiation from Ribbed Cylindrical Shell Excited by Single Radial Drive

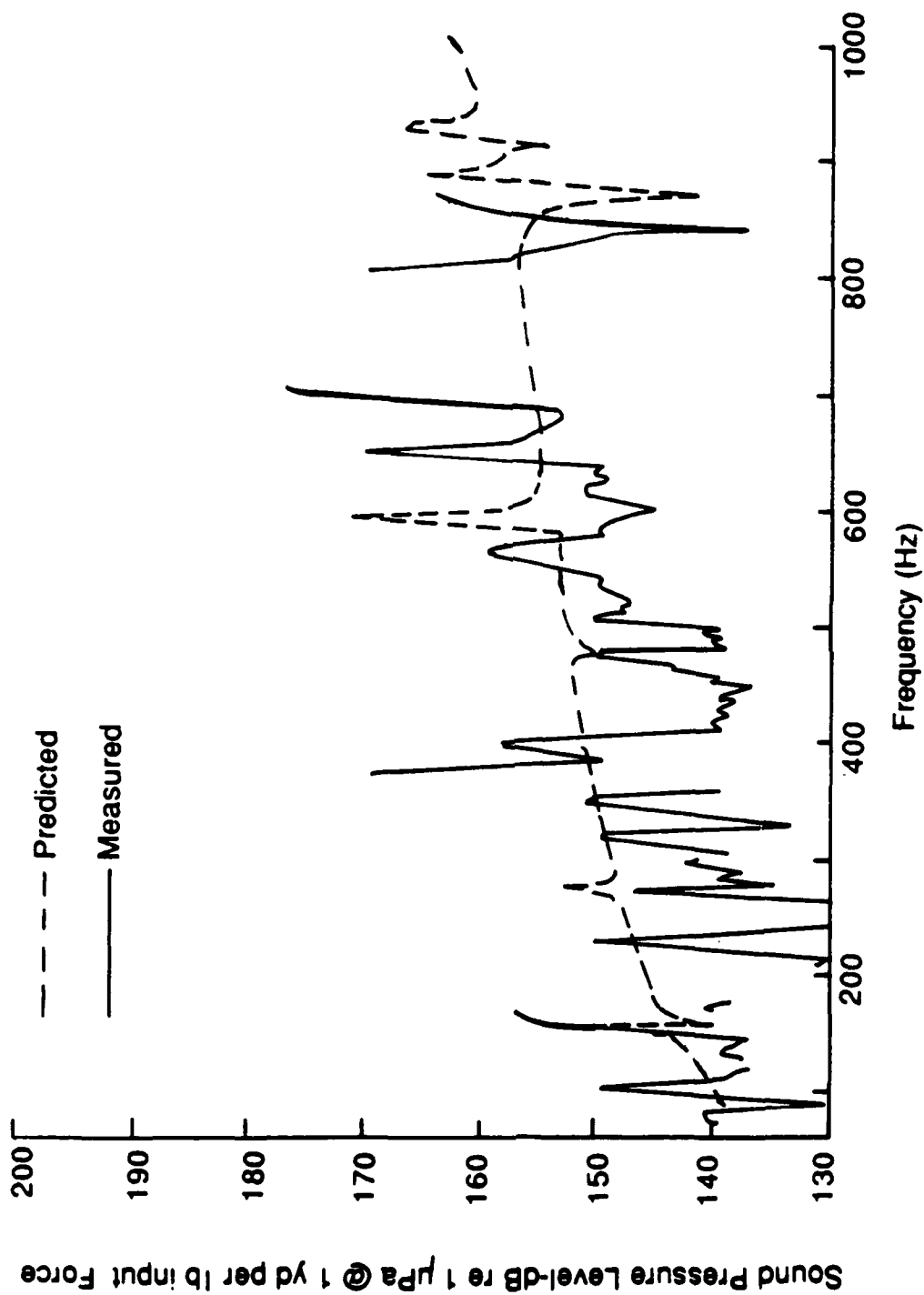


Figure 11. Comparison of Predicted and Measured Acoustic Radiation from Ribbed Cylindrical Shell Excited by Out-of-Phase Double Radial Drive

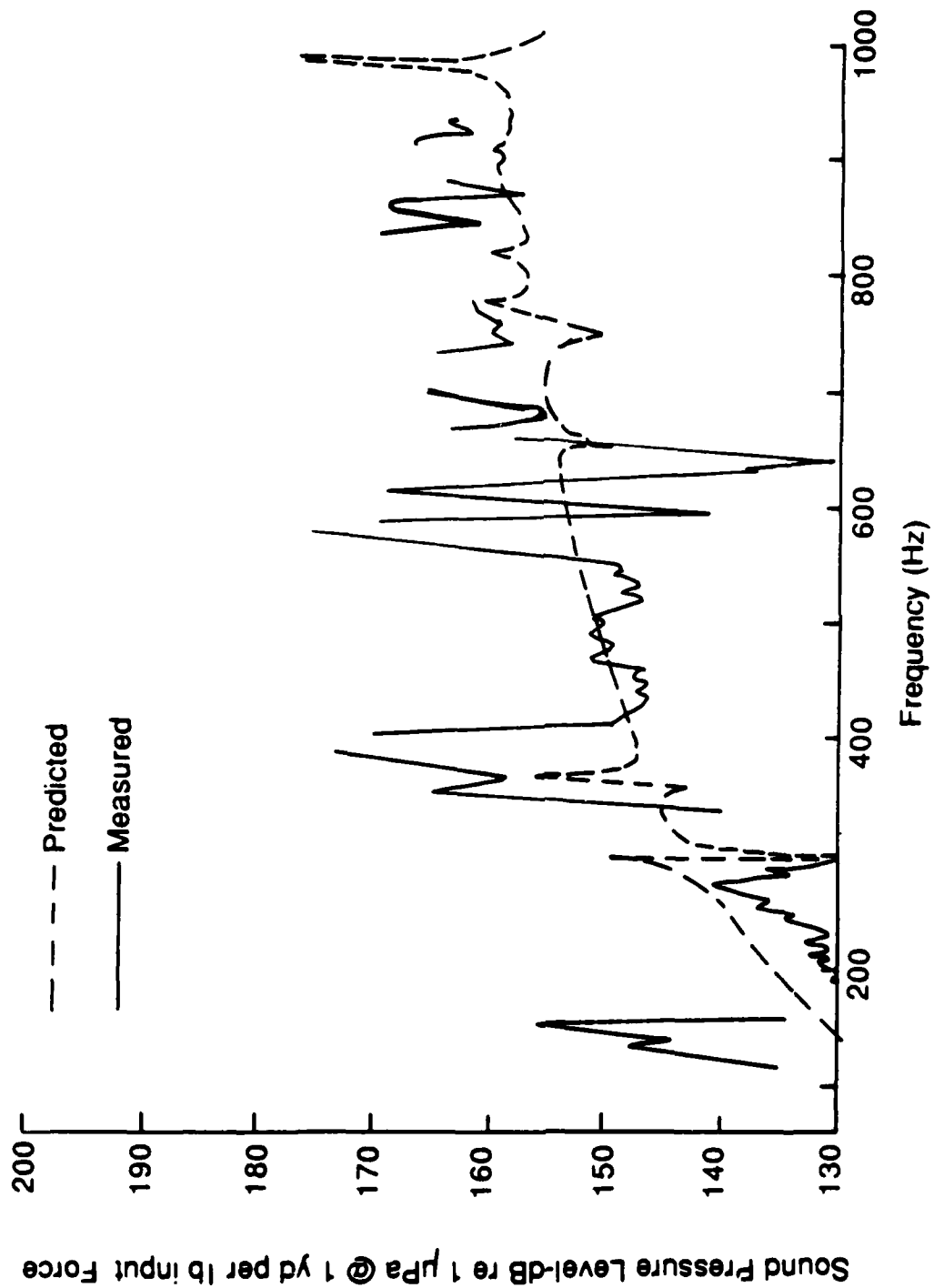


Figure 12. Comparison of Predicted and Measured Acoustic Radiation from Ribbed Cylindrical Shell Excited by In-Phase Double Radial Drive

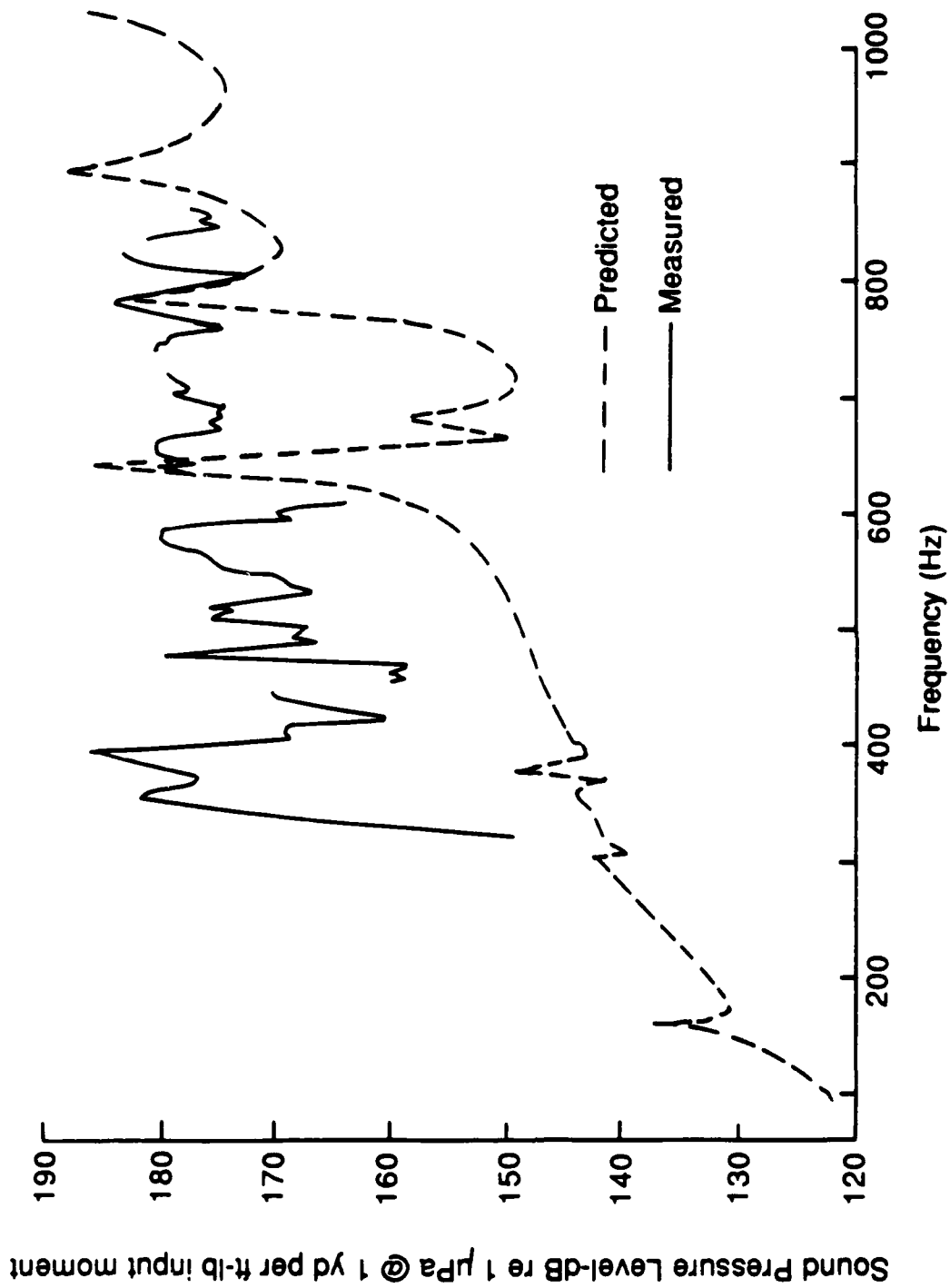


Figure 13. Comparison of Predicted and Measured Acoustic Radiation from Ribbed Cylindrical Shell Excited by Axial Moment Drive

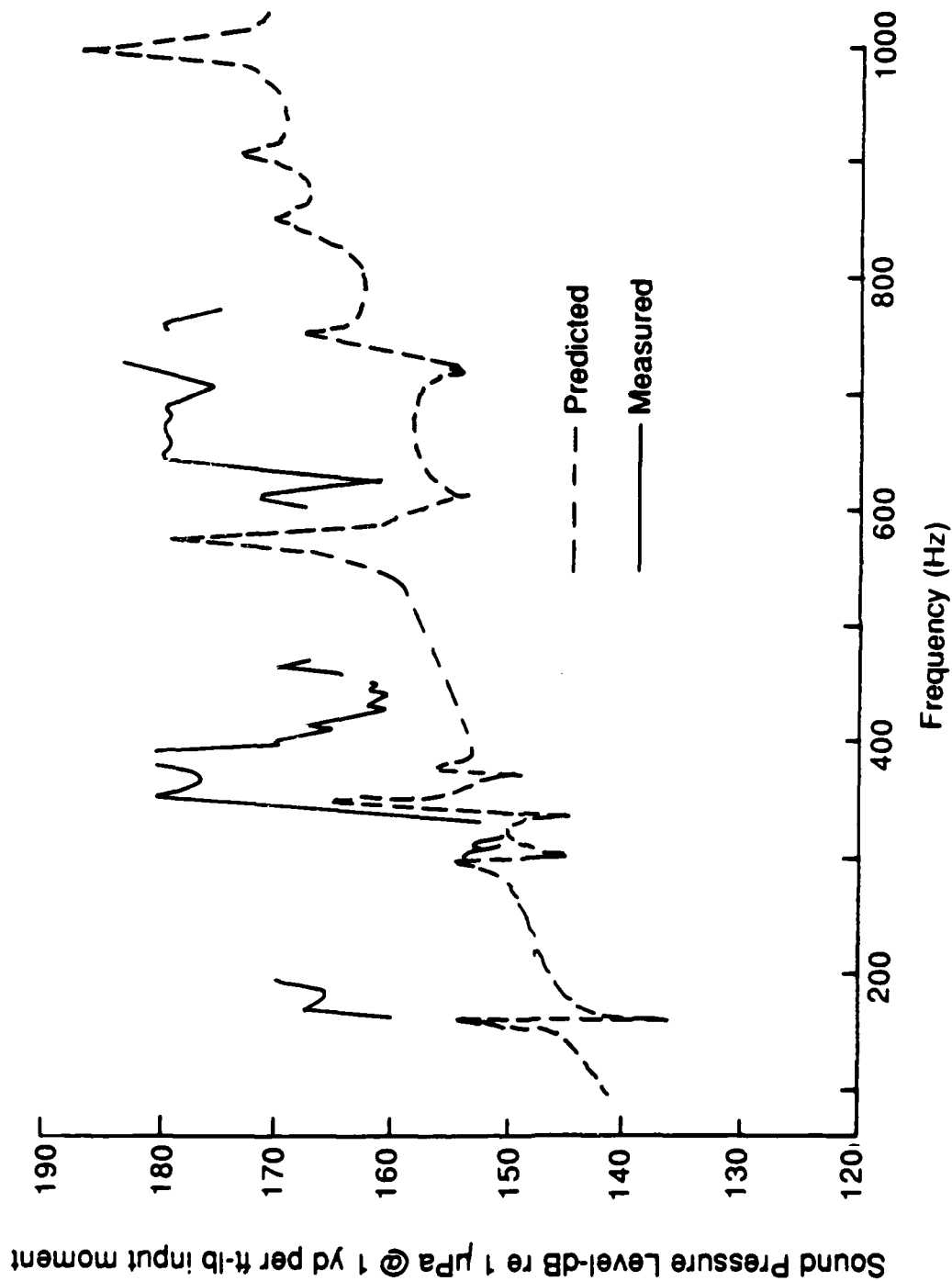


Figure 14. Comparison of Predicted and Measured Acoustic Radiation from Ribbed Cylindrical Shell Excited by Circumferential Moment Drive

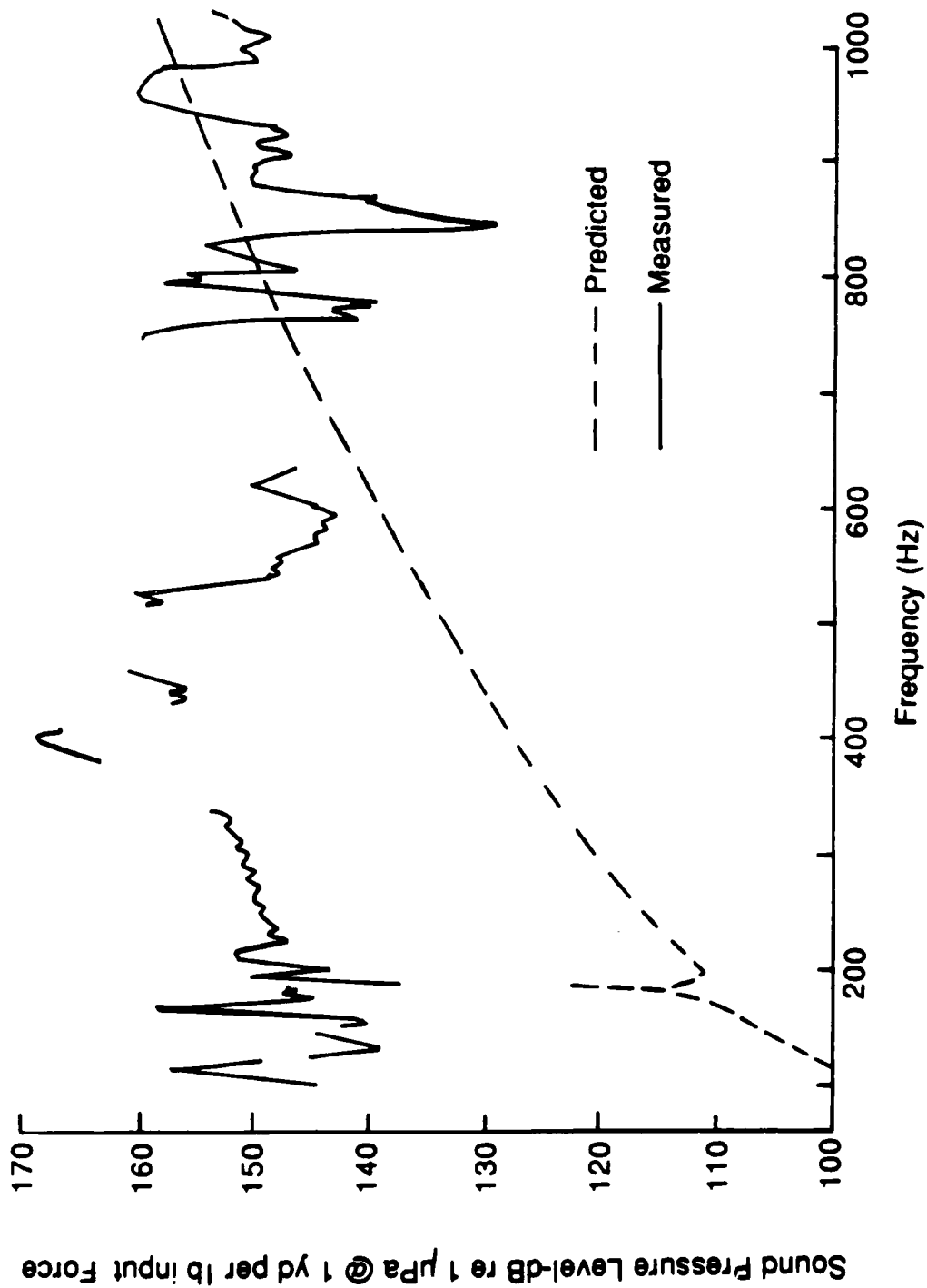


Figure 15. Comparison of Predicted and Measured Acoustic Radiation from Ribbed Cylindrical Shell Excited by Out-of-Phase In-Plane Circumferential Drive

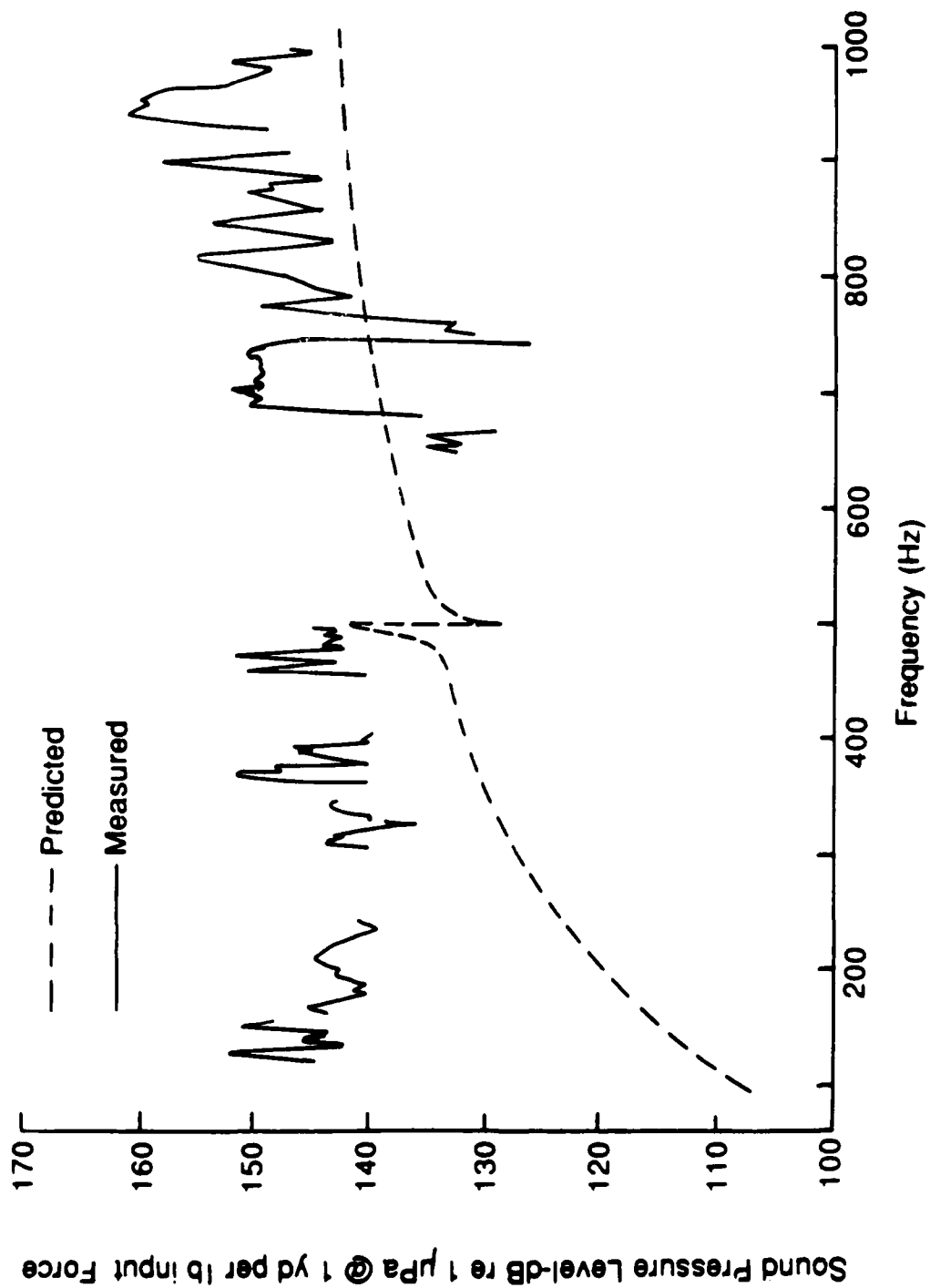


Figure 16. Comparison of Predicted and Measured Acoustic Radiation from Ribbed Cylindrical Shell Excited by In-Phase In-Plane Circumferential Drive

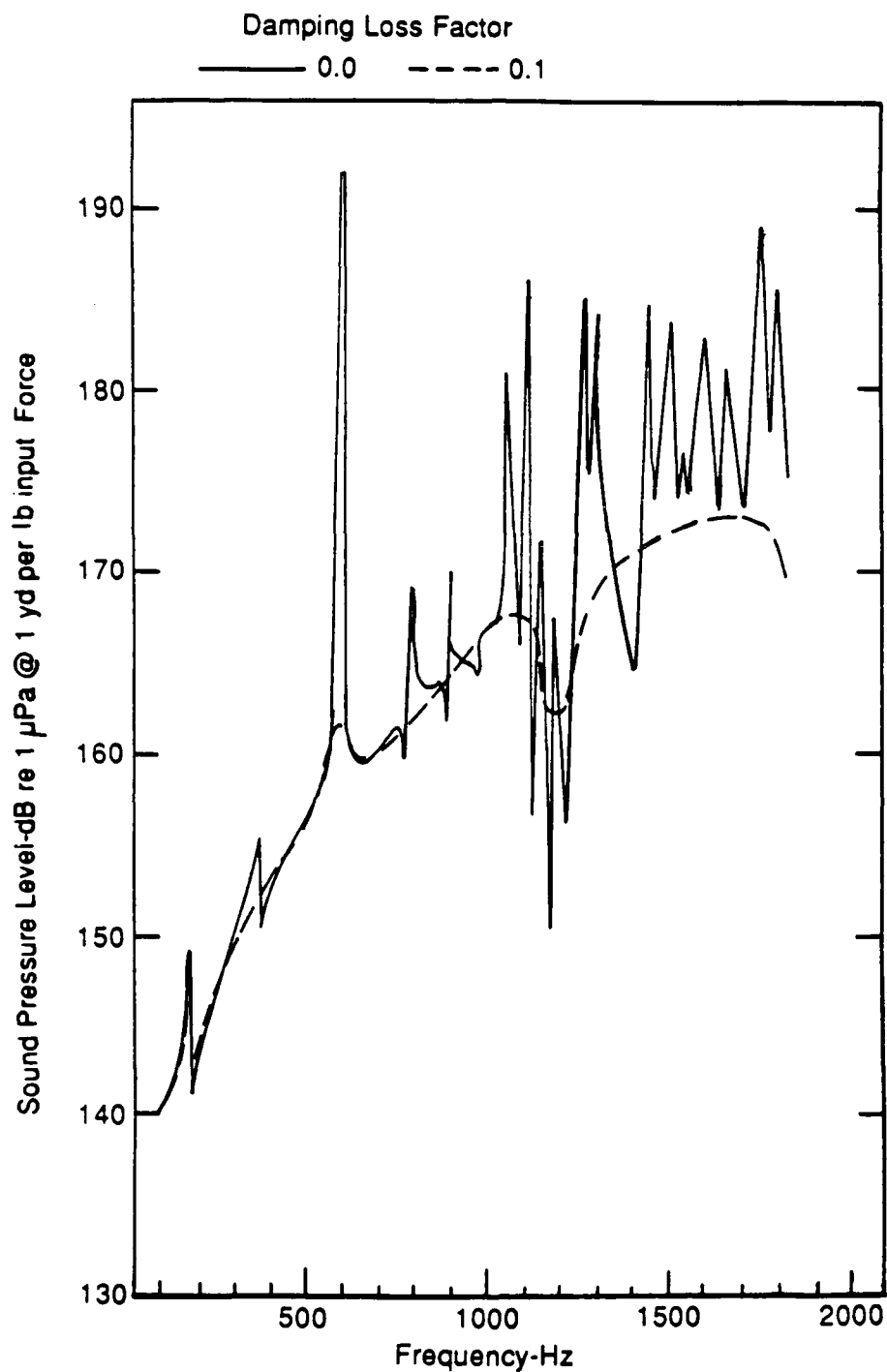


Figure 17. Acoustic Radiation from Doubly-Periodic Ribbed Shell with and without Damping for a Single Radial Drive

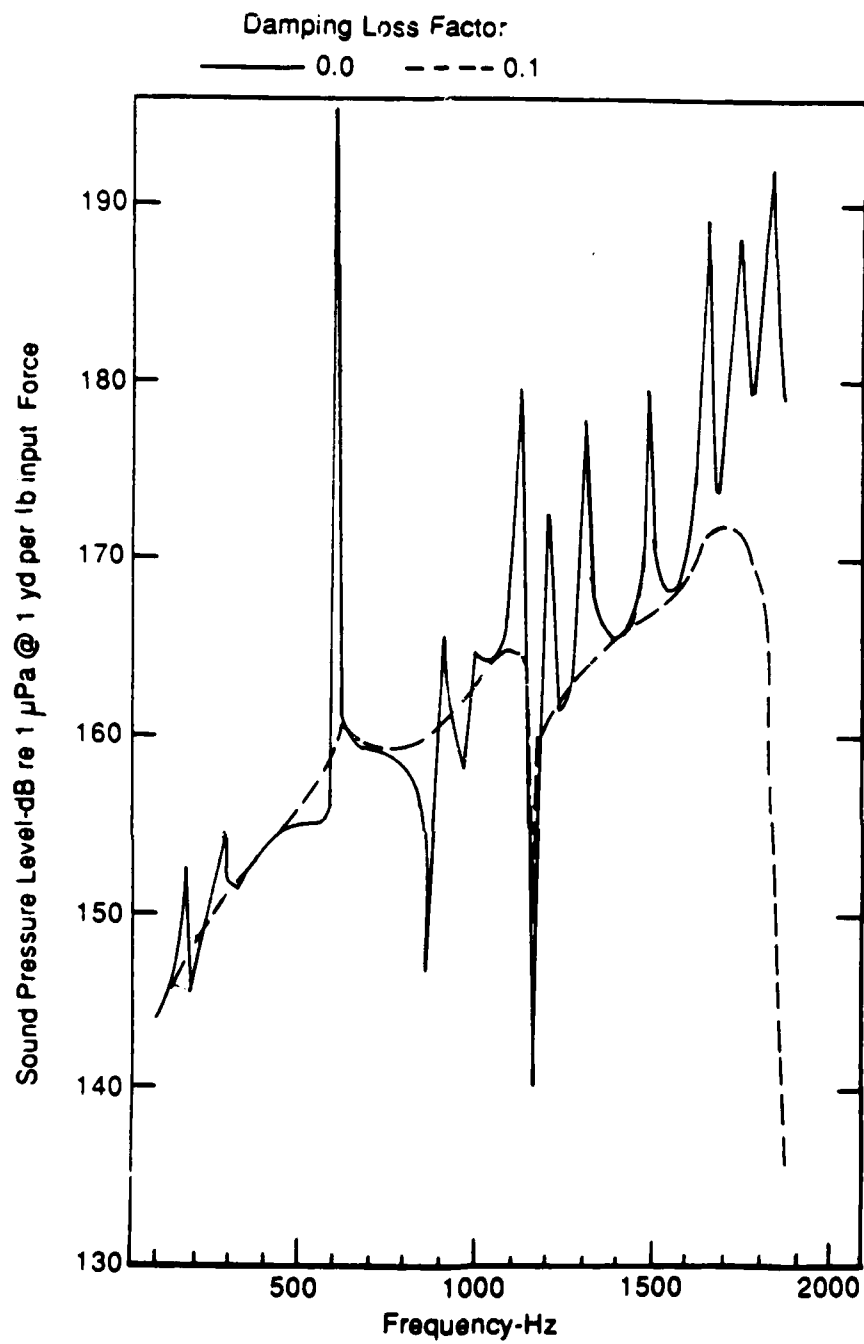


Figure 18. Acoustic Radiation from Doubly-Periodic Ribbed Shell with and without Damping for an Out-of-Phase Double Radial Drive

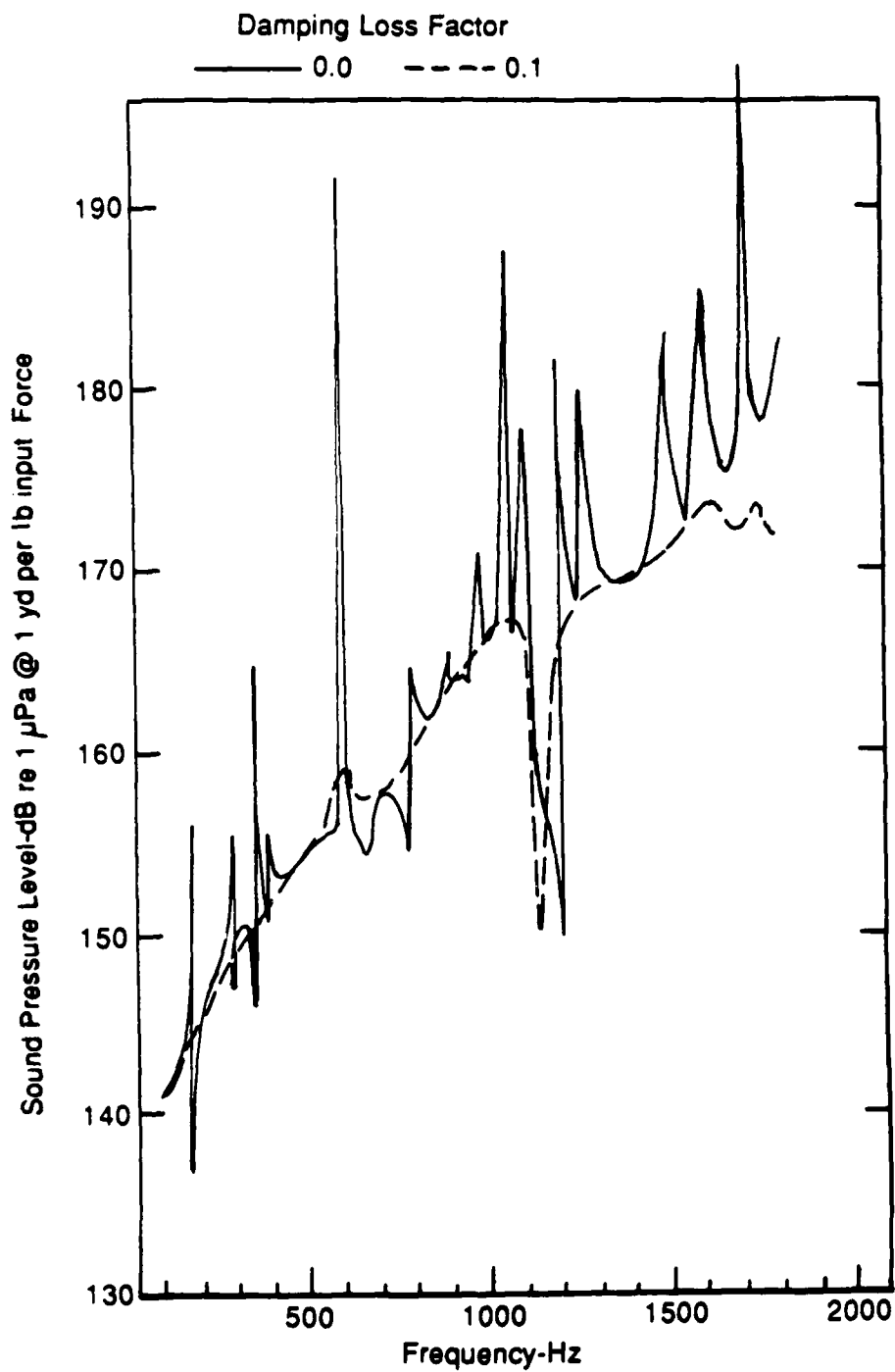


Figure 19. Acoustic Radiation from Doubly-Periodic Ribbed Shell with and without Damping for a Circumferential Moment Drive

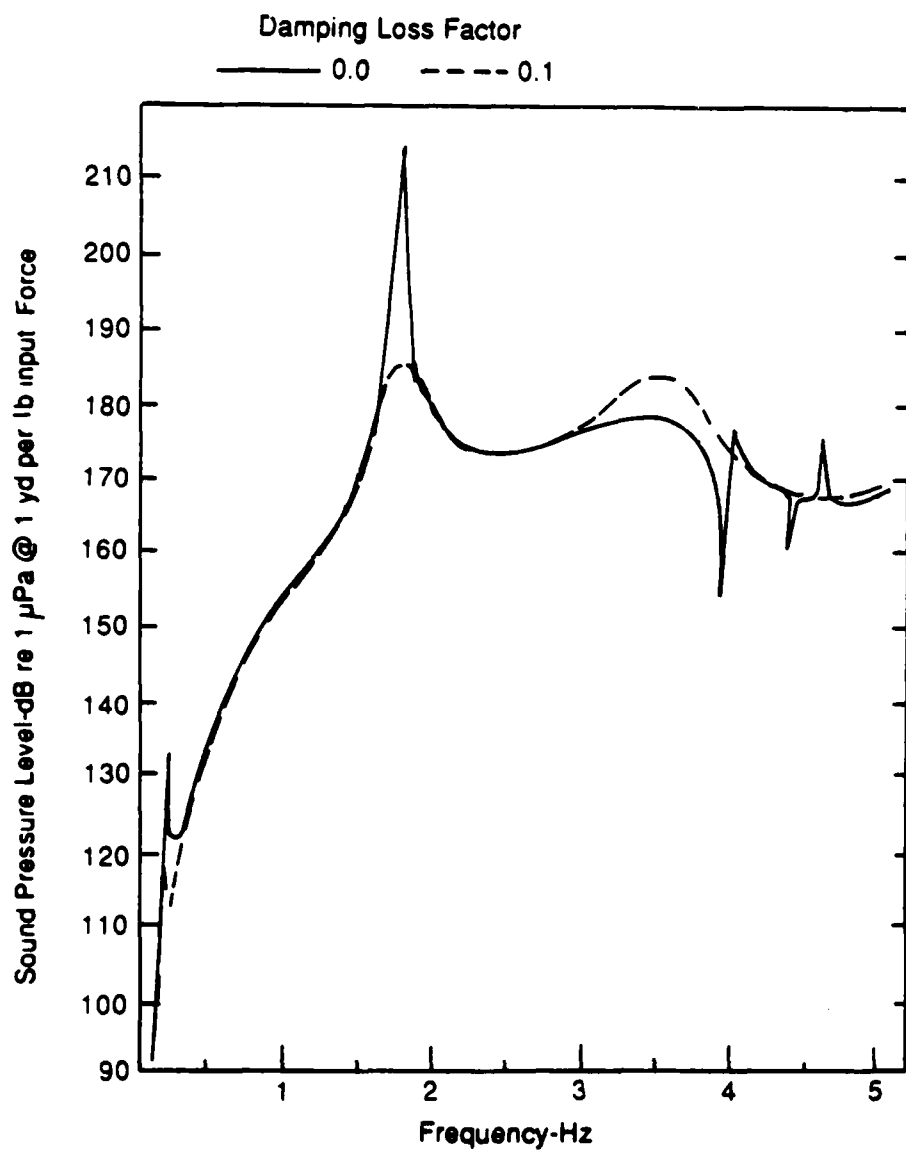


Figure 20. Acoustic Radiation from Doubly-Periodic Ribbed Shell with and without Damping for an Out-of-Phase In-Plane Circumferential Drive

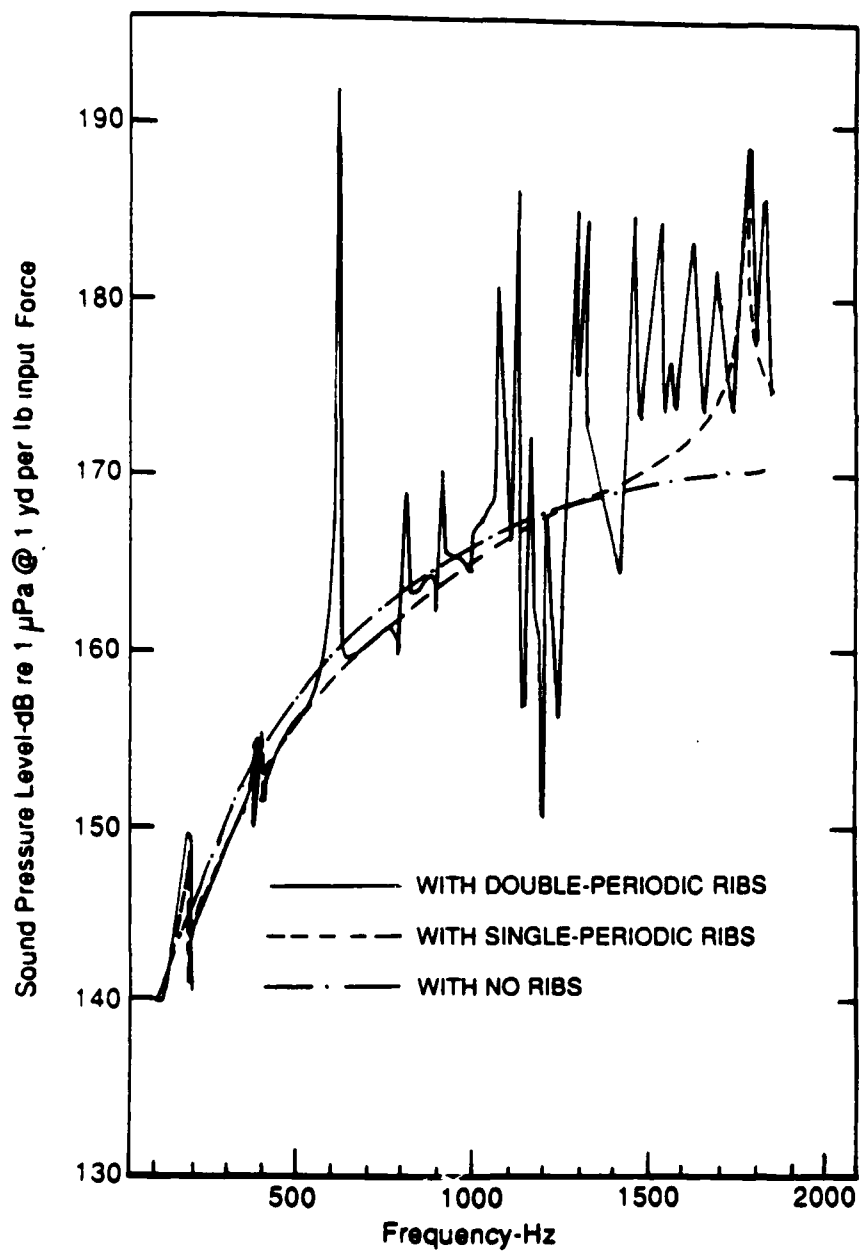


Figure 21. Acoustic Radiation from Shell with No Ribs, Singly-Periodic Ribs and Doubly-Periodic Ribs for Single Radial Drive

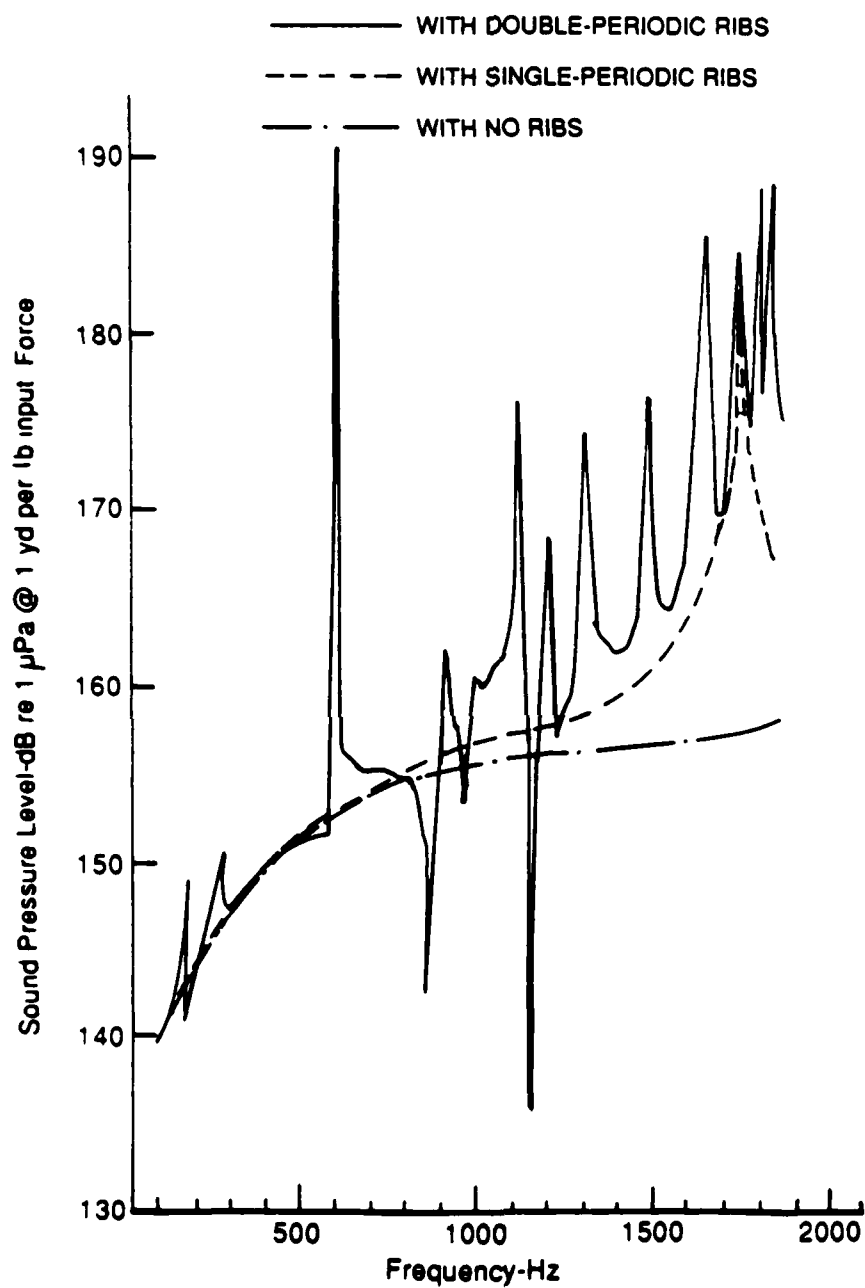


Figure 22. Acoustic Radiation from Shell with No Ribs, Singly-Periodic Ribs and Doubly-Periodic Ribs for Out-of-Phase Double Radial Drive

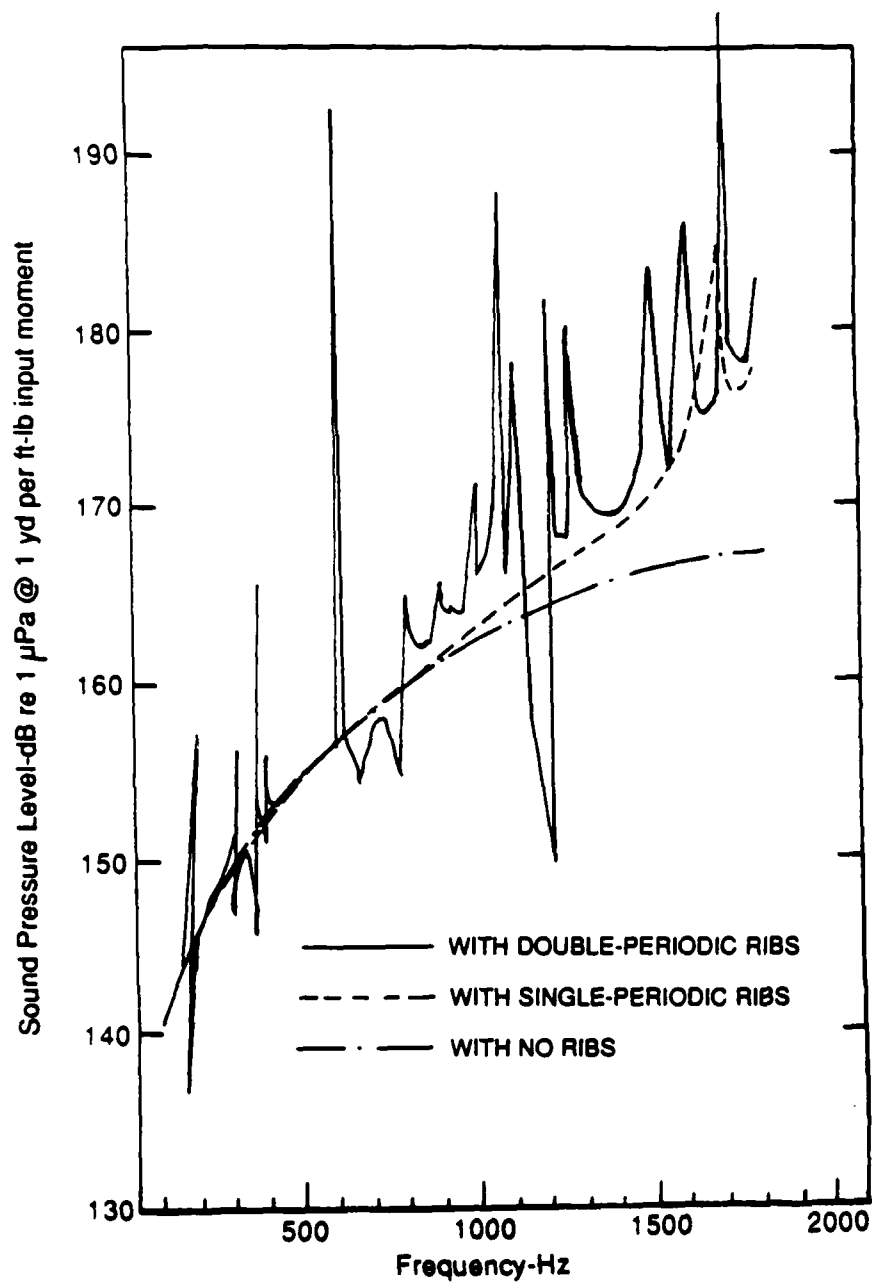


Figure 23. Acoustic Radiation from Shell with No Ribs, Singly-Periodic Ribs and Doubly-Periodic Ribs for Circumferential Moment Drive

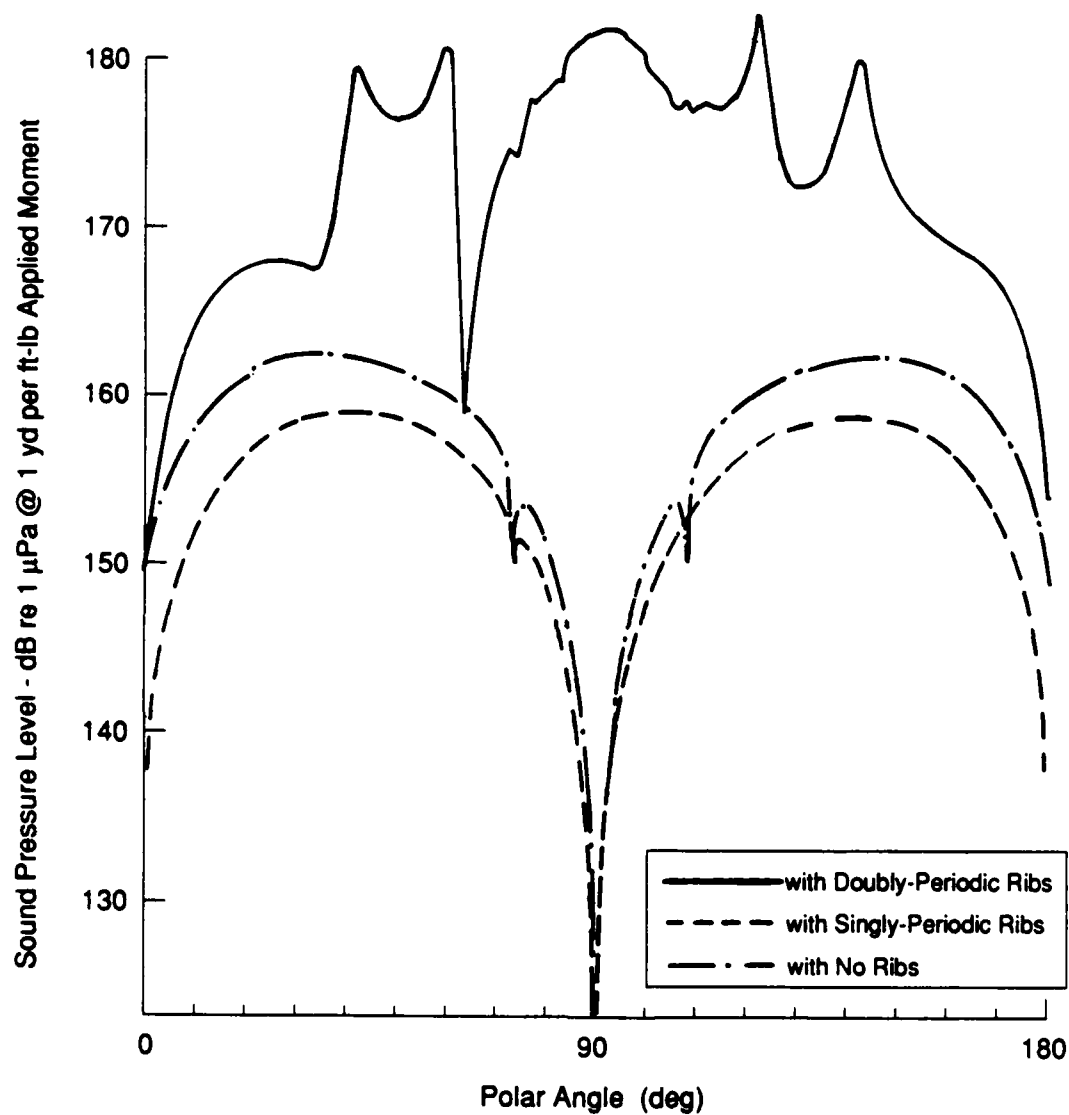


Figure 24. Acoustic Radiation Directivity for Shell with No Ribs, Singly-Periodic Ribs and Doubly-Periodic Ribs for Axial Moment Drive

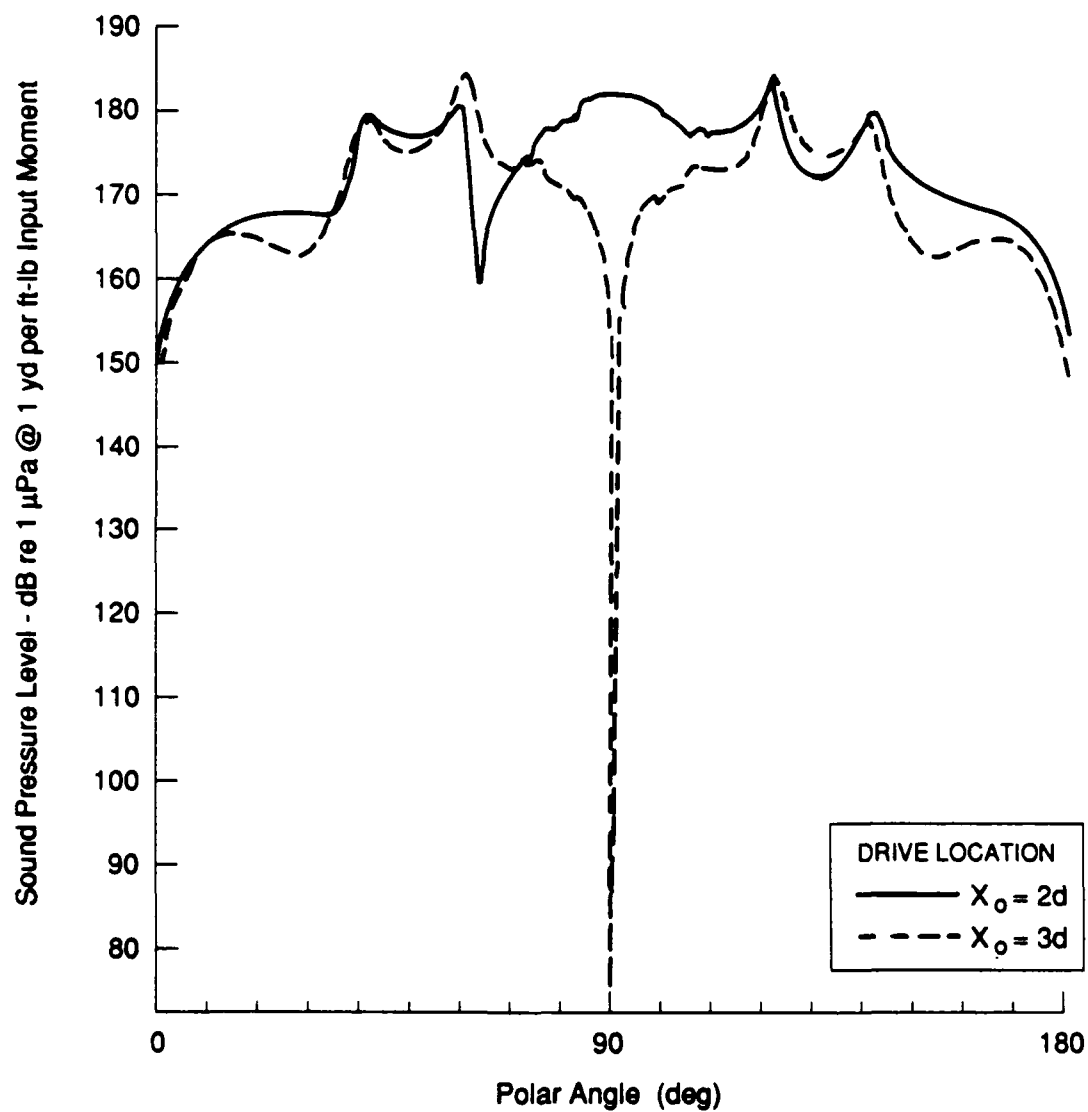


Figure 25. Acoustic Radiation Directivity for Doubly-Periodic Ribbed Shell for Axial Moment Drive at Different Locations

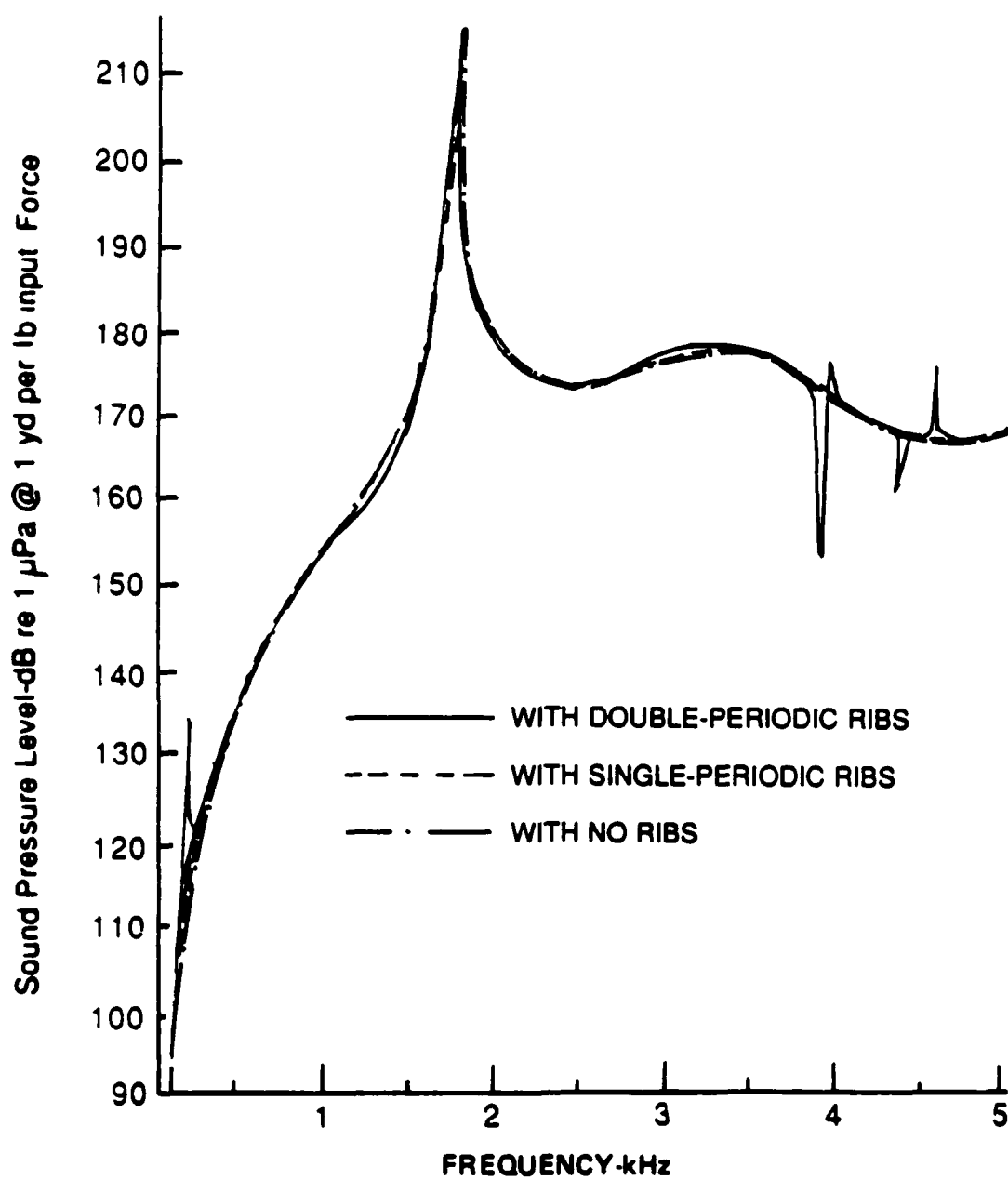


Figure 26. Acoustic Radiation from Shell with No Ribs, Singly-Periodic Ribs and Doubly-Periodic Ribs for In-Phase, In-Plane Circumferential Drive

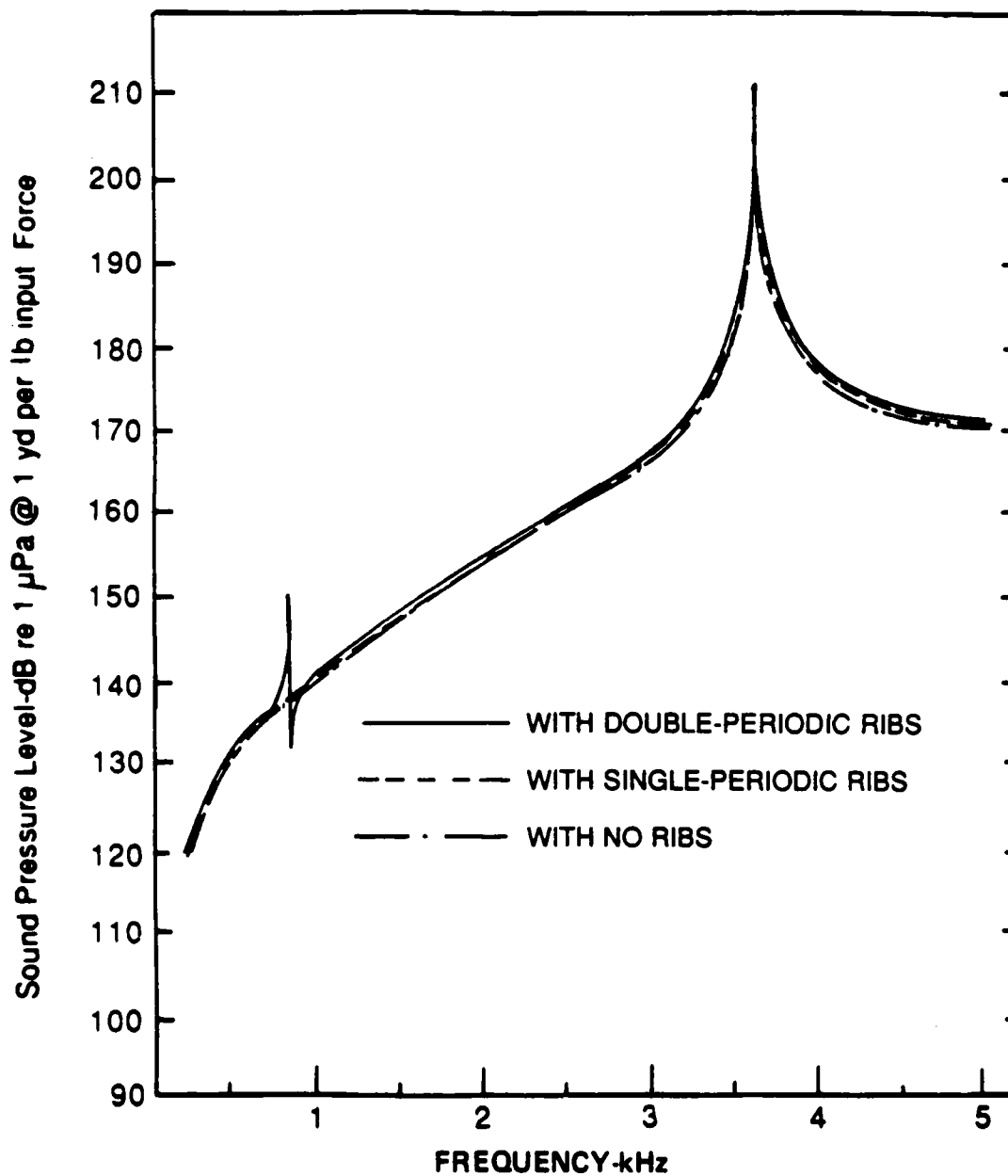


Figure 27. Acoustic Radiation from Shell with No Ribs, Singly-Periodic Ribs and Doubly-Periodic Ribs for Out-of-Phase, In-Plane Circumferential Drive

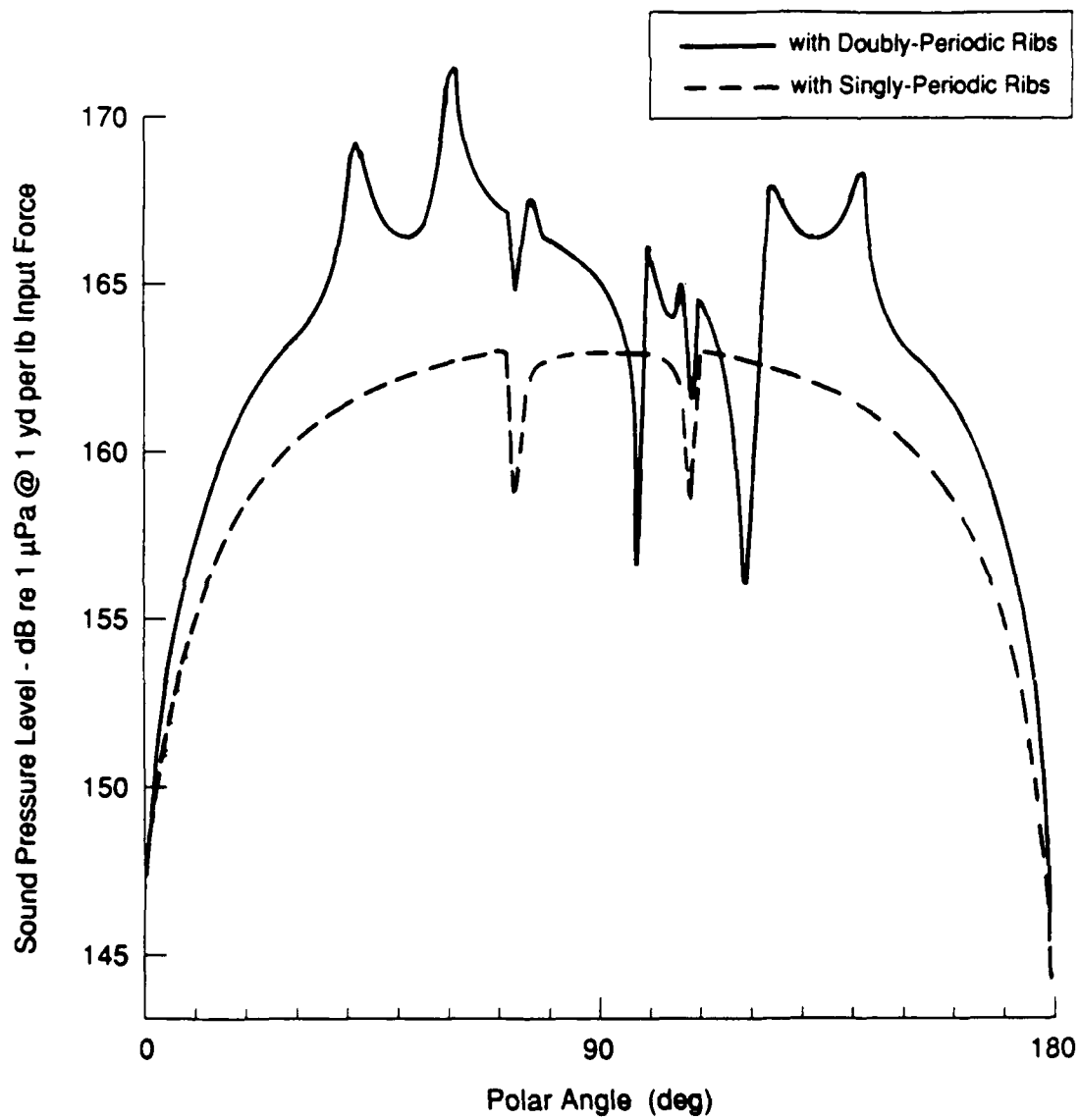


Figure 28. Acoustic Radiation Directivity for Shell with Singly- and Doubly-Periodic Ribs for Single Radial Drive

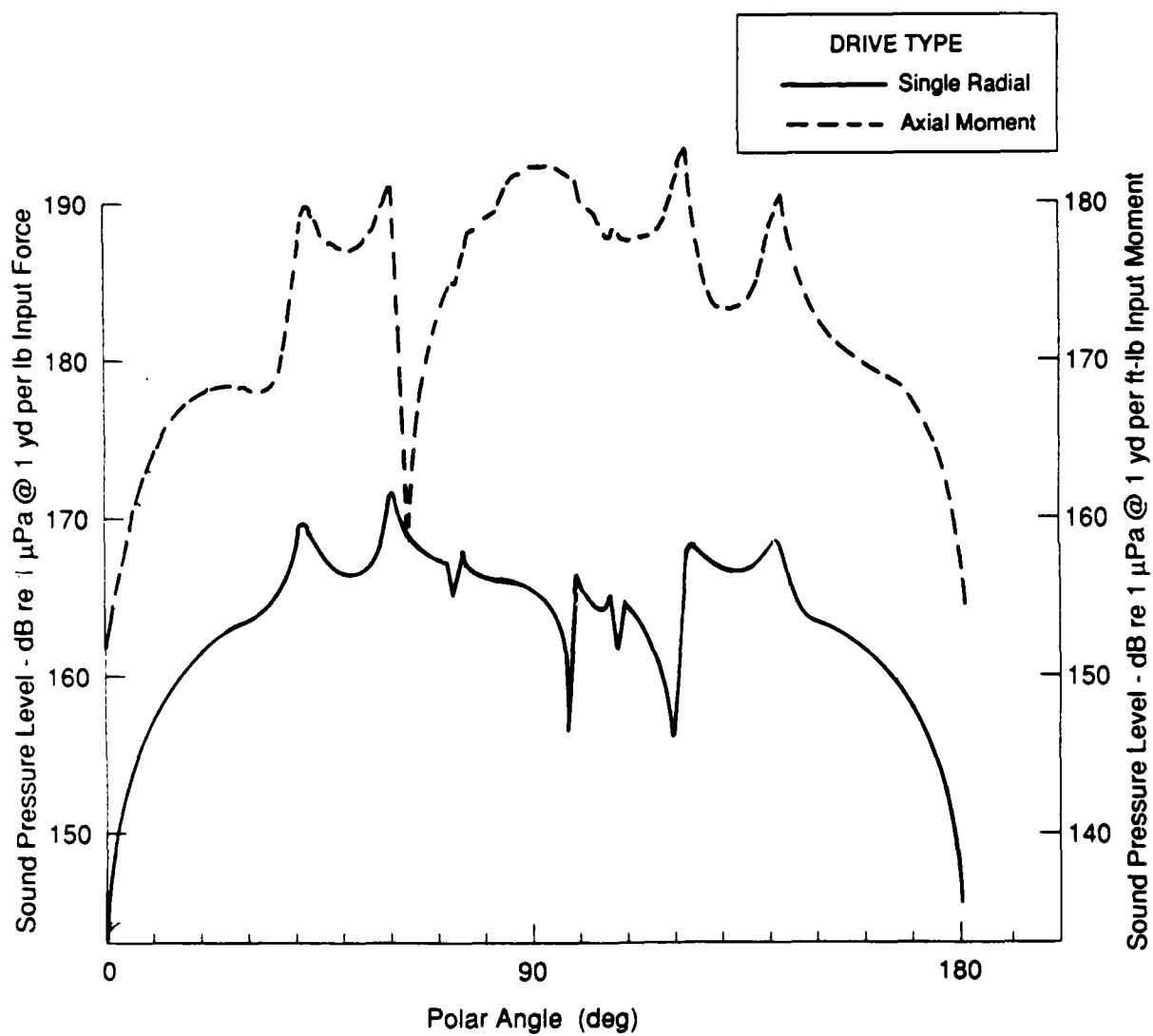


Figure 29. Acoustic Radiation Directivity for Doubly-Periodic Ribbed Shell for Single Radial and Axial Moment Drives

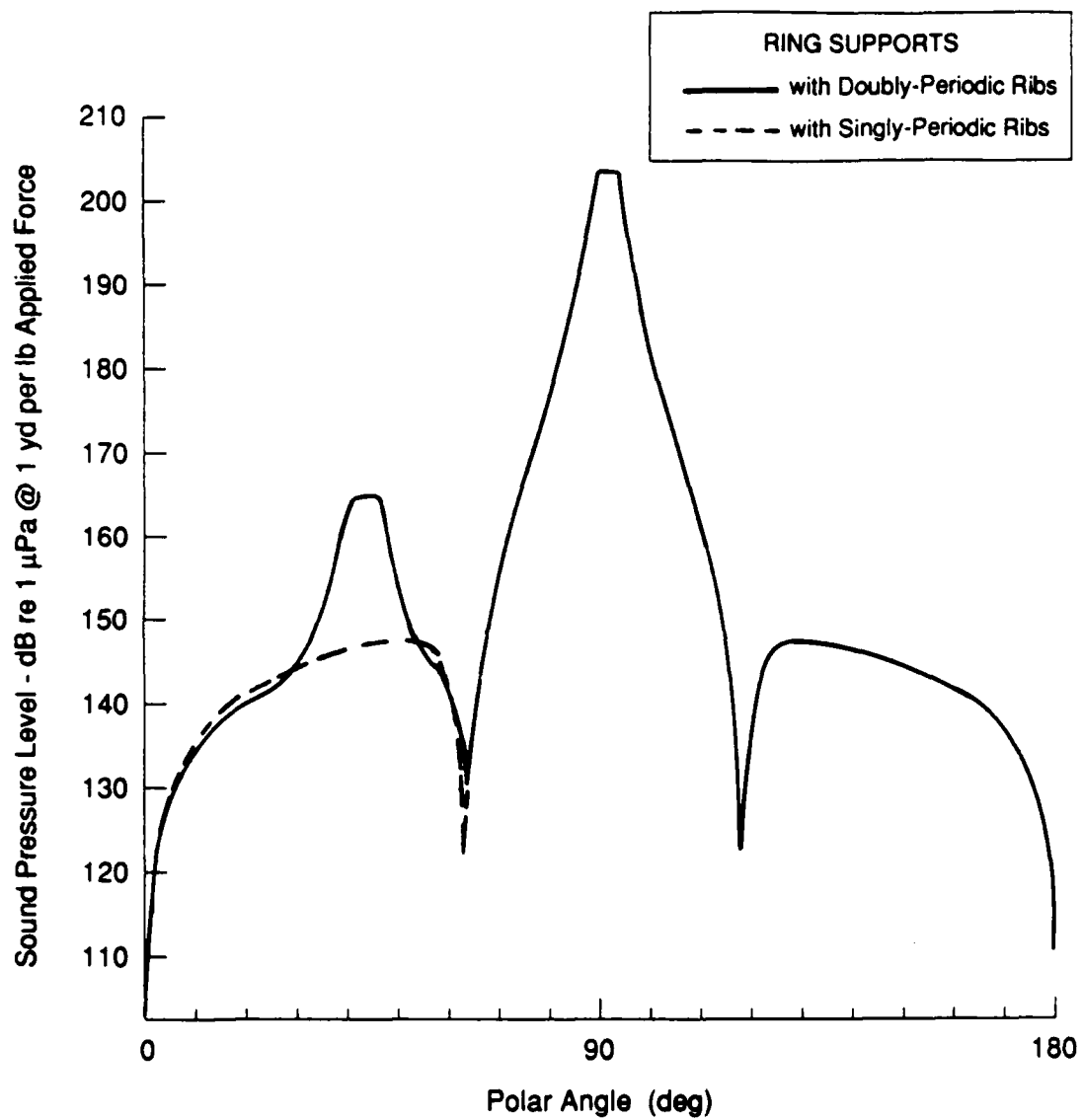


Figure 30. Acoustic Radiation Directivity for Shell with Singly- and Doubly-Periodic Ribs for In-Phase, In-Plane Circumferential Drive

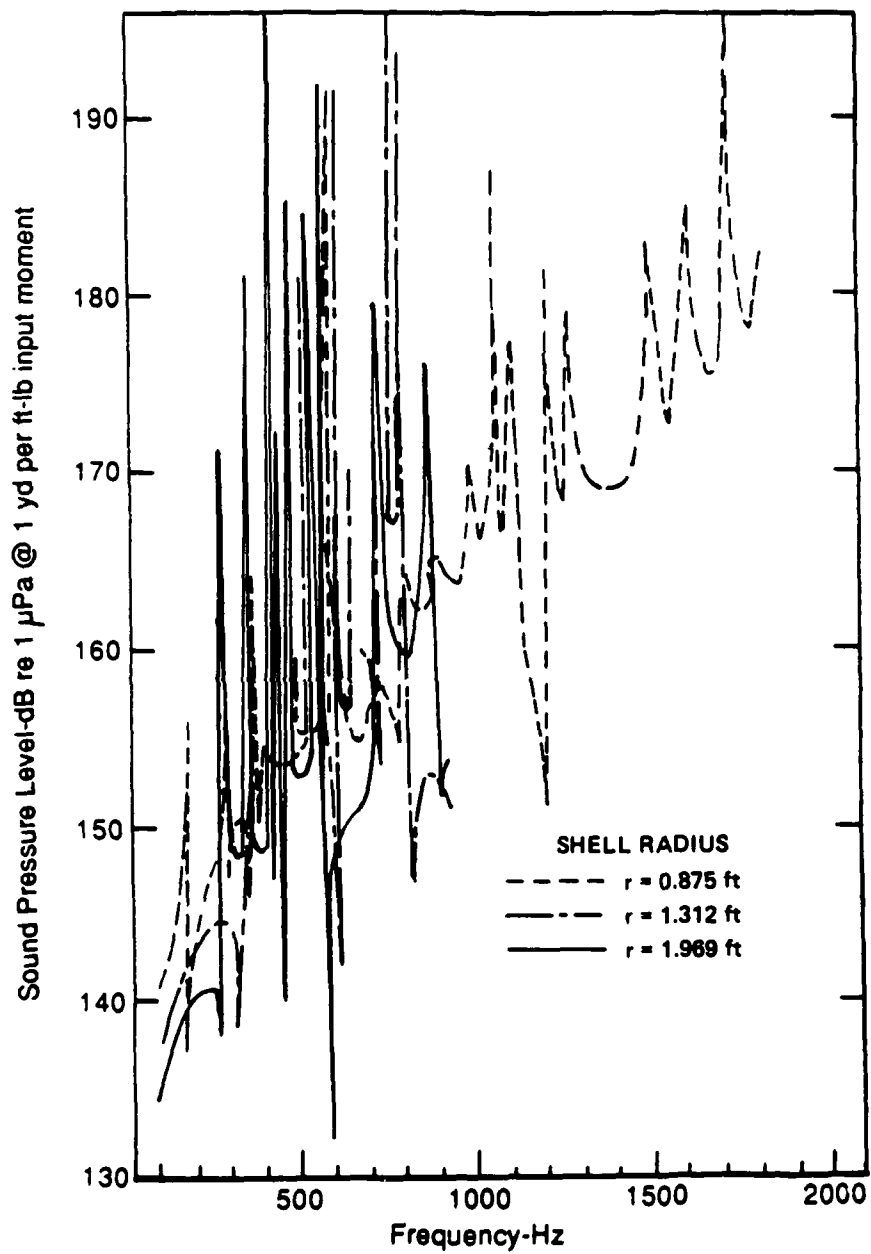


Figure 31. Acoustic Radiation from Doubly-Periodic Shell with Different Radii for Circumferential Moment Drive

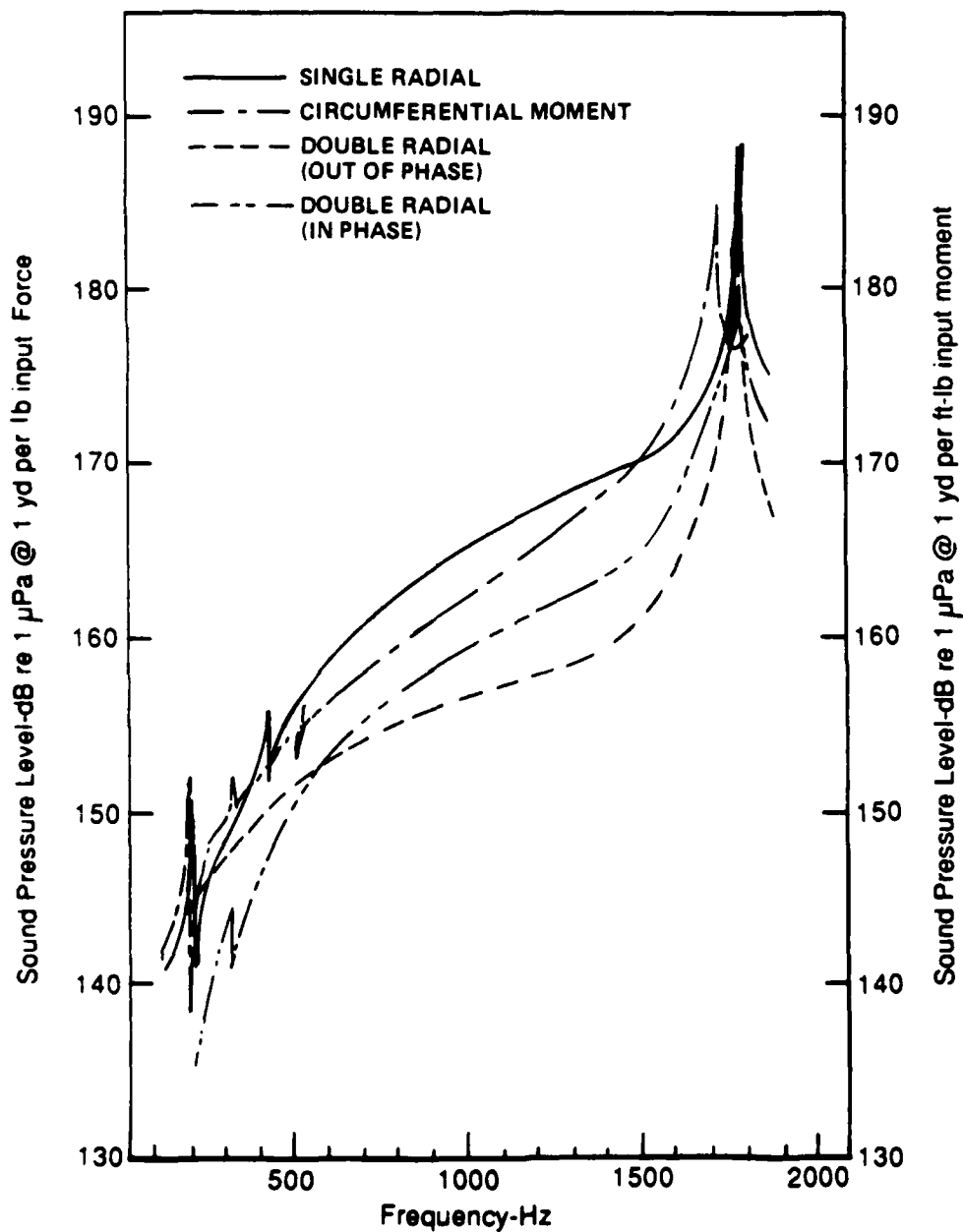


Figure 32. Acoustic Radiation from Singly-Periodic Ribbed Shell for Single Radial, Double In-Plane and Out-of-Phase Radial, and Circumferential Moment Drives

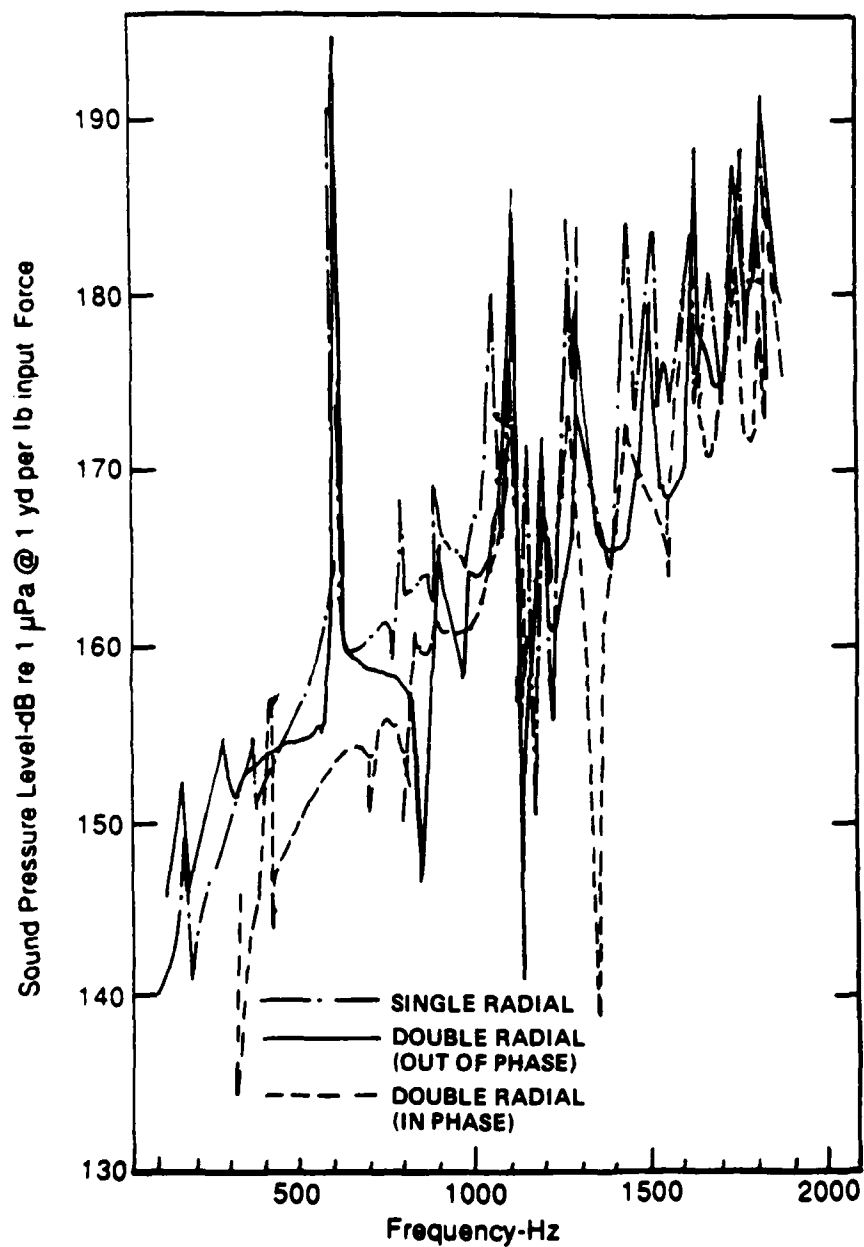


Figure 33. Acoustic Radiation from Doubly-Periodic Ribbed Shell for Single Radial and Double In-Phase and Out-of-Phase Radial Drives

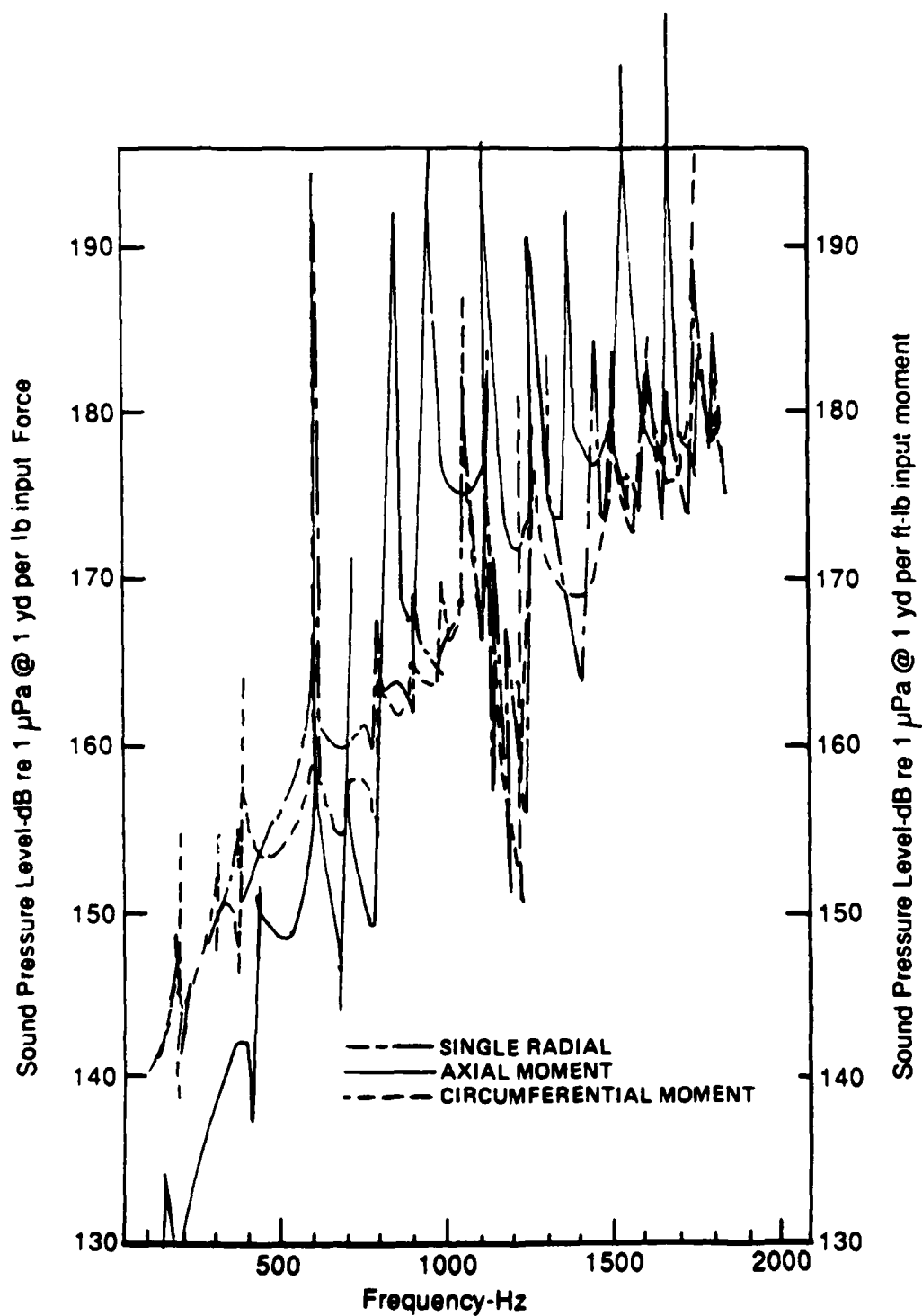


Figure 34. Acoustic Radiation from Doubly-Periodic Ribbed Shell for Single Radial, and Axial and Circumferential Moment Drives

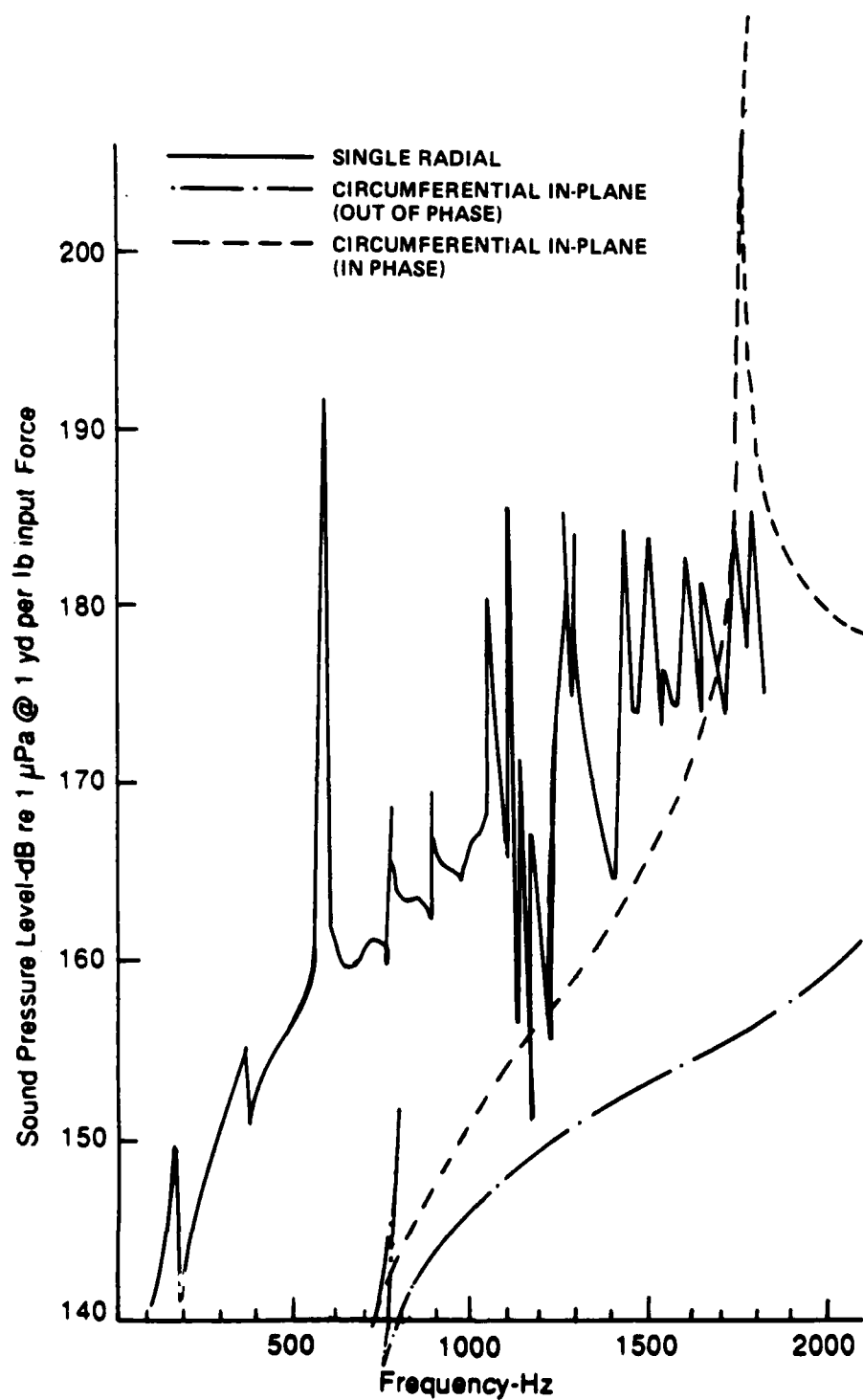


Figure 35. Acoustic Radiation from Doubly-Periodic Ribbed Shell for Single Radial, and Circumferential In- and Out-of-Phase, In-Plane Drives

DISTRIBUTION LIST FOR ARL PENN STATE TM 90-320 by C. B. Burroughs and
J. E. Hallander dated 14 January 1991

Office of Naval Research
Department of the Navy
800 North Quincy Street
Arlington, VA 2217
Attn: A. J. Tucker
Code 432
Copy No. 1

Defense Technical Information
Center
Building 5, Cameron Station
Alexandria, VA 22314
Attn: Library
Copy Nos. 2-3

Naval Research Laboratory
Washington, DC 20375
Attn: Library
Copy No. 4

David Taylor Research Center
Department of the Navy
Bethesda, MD 20084
Attn: Library
Copy No. 5

Naval Underwater Systems Center
Department of the Navy
Newport Laboratory
Newport, RI 02840
Attn: B. Sandman
Code 8215
Copy No. 6

AT&T
200 Laurel Avenue
Room 4F217
Middletown, NJ 07748
Attn: J. E. Hallander
Copy No. 7

Applied Research Laboratory
The Pennsylvania State University
P. O. Box 30
State College, PA 16804
Attn: C. B. Burroughs
Copy Nos. 8-9

Applied Research Laboratory
Attn: S. I. Hayek
Copy No. 10

Applied Research Laboratory
Attn: D. E. Thompson
Copy No. 11

Applied Research Laboratory
Attn: Water Tunnel Files
Copy No. 12

Applied Research Laboratory
Attn: ARL Library
Copy No. 13